

## Article

# Formation and Study of Bismuth Sulphide Thin Films on Textiles of Different Compositions

Veja Sruogaite and Valentina Krylova \* 

Department of Physical and Inorganic Chemistry, Kaunas University of Technology, Radvilenu Str. 19, LT-50254 Kaunas, Lithuania; veja.sruogaite@ktu.edu

\* Correspondence: valentina.krylova@ktu.lt

## Abstract

The study aimed to form thin  $\text{Bi}_2\text{S}_3$  films simultaneously on various textile materials using the environmentally friendly, low-cost successive ionic layer adsorption and reaction (SILAR) method at ambient temperature, and to evaluate the influence of the textile's composition on the resulting composites' surface phase composition, morphology, and optical properties. The deposited films were characterised using X-ray diffraction (XRD), scanning electron microscopy (SEM), energy dispersive X-ray (EDX) spectroscopy, and ultraviolet–visible (UV-Vis) diffuse reflectance spectroscopy. This paper discusses how the structure and composition of the textiles affect the phase and elemental composition, crystallinity, morphology and optical properties of the formed films. The properties of the films are then compared. Depending on the textiles used, the formed films can be amorphous or polycrystalline, and can be rich in sulphur or near stoichiometric. Accordingly, the normalised atomic percentages of Bi in the films range from 3.62% to 33.87%, and those of S range from 96.38% to 66.13%. The optical energy gap value of the composites also varies depending on the textile substrate, ranging from  $E_g = 1.58$  eV to  $E_g = 1.8$  eV. These properties directly impact the films' applications. We have obtained a rather low value of the optical energy gap in a simpler way.

**Keywords:** bismuth(III) sulphide films; structural textile; SILAR; SEM; optical properties



Academic Editors: Manuel Filipe P. C. M. Costa and Sandra Franco

Received: 18 August 2025

Revised: 5 September 2025

Accepted: 8 September 2025

Published: 10 September 2025

**Citation:** Sruogaite, V.; Krylova, V. Formation and Study of Bismuth Sulphide Thin Films on Textiles of Different Compositions. *Appl. Sci.* **2025**, *15*, 9904. <https://doi.org/10.3390/app15189904>

**Copyright:** © 2025 by the authors. Licensee MDPI, Basel, Switzerland. This article is an open access article distributed under the terms and conditions of the Creative Commons Attribution (CC BY) license (<https://creativecommons.org/licenses/by/4.0/>).

## 1. Introduction

Solar photovoltaic (PV) systems are supplying an increasing share of the global electricity market. The majority employ crystalline silicon solar cells (SCs), characterised by rigidity, brittleness, and the high processing cost of silicon. Perovskite photoelectrochemical solar cells (SEs) offer simpler designs but face challenges related to high costs and instability of organic semiconductors used for charge transfer. These systems are also unsuitable for lightweight, flexible PV applications. Textile-based flexible PV systems have emerged as an alternative, inspired by textiles' excellent performance in electronic devices. Selecting appropriate textiles and semiconductors is critical for developing efficient flexible PV structures.

Currently, various textiles are being used: polytetrafluoroethylene (PTFE)-coated glass fibre (GF), mesh or aramid fabric, silicone-coated fibreglass fabric, polyvinylchloride (PVC)-coated polyester (PES) fabric, etc. PTFE-coated aramid fabric is a composite material that combines the high-performance characteristics of aramid fibres with the non-stick and heat-resistant properties of PTFE coating. This combination makes it suitable for industrial

applications where strength and heat resistance are essential. Silicone-coated fibreglass fabric is made of E-Glass fibreglass base fabric and high-purity silicone coating.

Electrically conductive textiles are produced from woven or knitted conductive yarns. Conductivity can also be imparted by sewing, embroidery, chemical coatings, or surface metallisation with silver, nickel, or copper nanoparticles. These fabrics typically exhibit electrical resistance below  $1 \Omega/\text{sq}$  [1].

Semiconductor thin films are being investigated for textile integration to develop smart, functional building materials. When deposited on fabrics such as polyester or cotton, they enhance durability, conductivity, and energy efficiency. Nanocrystalline semiconductors are of particular interest for advanced electronic and optoelectronic applications. Among these, metal sulphides stand out due to their broad utility in electronics, energy storage and conversion, optics, electrochemical sensing, photocatalysis, and biomedicine, enabled by their unique structural and optical properties [2–5].

Bismuth(III) sulphide ( $\text{Bi}_2\text{S}_3$ ) is used in the following: photovoltaic converters, photocatalysts [6], thermoelectric cooling technologies based on the Peltier effect [7], hydrogen storage [8], thermoelectric gas sensors [9,10], optical detection for IR and UV light [11,12], photoelectrochemical solar cells (SEs), electronic and optoelectronic devices [7], lithium-ion batteries [13], memristors [14], and cancer diagnostics [15,16].  $\text{Bi}_2\text{S}_3$  is an n-type crystalline semiconductor with intrinsic properties like: low direct optical energy gap (1.3–1.7 eV), which is within optimal range for the solar spectrum, high absorption coefficient ( $10^4$ – $10^5 \text{ cm}^{-1}$ ), high ionic conductivity, and sufficient conversion efficiency of incident photons to electrons ( $\sim 5\%$ ) [17], making it ideal for solar energy conversion devices [18]. It has an orthorhombic, layered (lamellar) structure that is held together by weak Bi–S bonds. Some examples of bismuth sulphide nanostructures include belts, stars, spheres, ribbons, snowflakes, flowers, rods, tubes, and wires [19–23]. This van der Waals material has potential as a solar absorber, and its use in optoelectronics is the subject of extensive research [24].

Deposition of thin  $\text{Bi}_2\text{S}_3$  includes the following: thermal evaporation [25], chemical vapour deposition [26], solvothermal synthesis [27], the ultrasonic method [28], pulsed laser deposition [29], microwave irradiation [22], spray pyrolysis [30], and electrodeposition [31]. These methods of forming  $\text{Bi}_2\text{S}_3$  thin films are disadvantageous because of the requirement for high temperatures and ultrahigh vacuums, as they are cost-inefficient.

The chemical methods, chemical bath deposition (CBD) [32] and successive ion layer adsorption and reaction (SILAR) [33], are promising due to their user-friendly equipment, low cost, and ability to deposit over a large surface area. The main advantage is the ability to control the reaction rate and film thickness.

The predominantly used cationic precursor in chemical deposition methods for bismuth-containing thin film fabrication is bismuth nitrate pentahydrate [32,33]. Sulphur-containing precursors—thiourea, thiosulphate, thioacetamide [34], hydrogen sulphide [7], sodium sulphide, and elemental sulphur—are commonly used in chemical deposition of bismuth sulphide [35].

During CBD film formation, the substrate and all cationic and anionic precursors are in the same reaction bath—the deposited materials adhere to the substrate and the bath. The SILAR method involves immersion of the substrate in different reaction baths containing either cationic or anionic precursors. Thin film is deposited exclusively on the substrate. The absence of a complexing agent results in highly pure films. This constitutes one deposition cycle. The rate of deposition is controlled by adjusting the concentration of the precursor solutions. Film thickness is controlled by the immersion time and the number of cycles. This enables simultaneous control of film deposition. In this study, the SILAR method was chosen to form thin  $\text{Bi}_2\text{S}_3$  films.


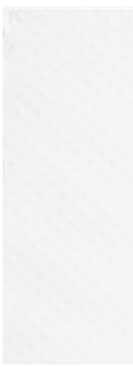



The study aimed to form thin  $\text{Bi}_2\text{S}_3$  films simultaneously on various textile materials using the SILAR method, and to evaluate the influence of the textile's composition on the resulting composites' surface phase composition, morphology, and optical properties.

## 2. Materials and Methods

### 2.1. Materials

For the deposition of bismuth sulphide thin films, 5 samples of textiles with different compositions were selected: polyethylene terephthalate fabric coated with polyvinyl chloride (PET/PVC, Verseidag-Indutex GmbH, Krefeld, Germany), glass fibre fabric coated with polytetrafluoroethylene (GF/PTFE, Verseidag-Indutex GmbH, Krefeld, Germany), cotton/polyester/spandex (C/PES/S, Mianyang Jialian Printing and Dyeing Co., Ltd., Mianyang, China), polyamide/silver (PA/Ag, Kufner Holding GmbH, Unterhaching, Germany), and polyamide/copper (PA/Cu, Kufner Holding GmbH, Unterhaching, Germany). The textile samples were cut into  $(2 \times 7) \text{ cm}^2$  samples. Table 1 lists the composition of each textile sample, along with photographs and the technical data provided by the manufacturer.

**Table 1.** Photographs of samples and technical data of textiles provided by manufacturers.

Textile	GF/PTFE	PET/PVC	C/PES/S	PA/Cu	PA/Ag
Photographs					
Composition	PTFE-coated fibreglass	PET yarn, coating PVC, filler <sup>1</sup>	75% cotton (C), 24% polyester (PES), 1% spandex (S) <sup>2</sup>	100% nylon (PA), metallisation copper (Cu)	100% nylon (PA), metallisation silver (Ag)
Thickness, mm	0.58	0.56	0.35	0.05	0.10
Basis weight, g/m <sup>2</sup>	1100	850	290	52	34
Heat resistance, °C	260	70	80	30	30
Cold resistance, °C	−73	−30	−30	−30	−30

<sup>1</sup> The filler pigment is not specified, but XRD analysis showed that the dominant inorganic fillers are  $\text{CaCO}_3$  and  $\text{TiO}_2$  (XRD results are presented in Section 3.2.2). <sup>2</sup> The spandex fibre that is most used has at least 85% polyurethane and 15% other materials, like nylon or polyester, in it.

The following reagents were used to prepare the etching solutions: chromium(VI) oxide ( $\text{CrO}_3$ ,  $\geq 97 \text{ wt\%}$ , Sigma-Aldrich Chemie GmbH, Munich, Germany), sulphuric acid ( $\text{H}_2\text{SO}_4$ ,  $\geq 96 \text{ wt\%}$ , Barta a Cihlar, Rožnov pod Radhoštěm, Czech Republic), and orthophosphoric acid ( $\text{H}_3\text{PO}_4$ ,  $\geq 60 \text{ wt\%}$ , Lach-Ner, Ltd., Neratovice, Czech Republic). Bismuth nitrate ( $\text{Bi}(\text{NO}_3)_3 \cdot 5\text{H}_2\text{O}$ ,  $\geq 99 \text{ wt\%}$ , Sigma-Aldrich Chemie GmbH, Munich, Germany) and sodium thiosulphate ( $\text{Na}_2\text{S}_3\text{O}_3 \cdot 5\text{H}_2\text{O}$ ,  $> 98 \text{ wt\%}$ , Sigma-Aldrich Chemie GmbH, Munich, Germany) were used to prepare solutions for the deposition of bismuth sulphide thin films.

### 2.2. Thermo-Oxidative Acid Treatment of GF/PTFE and PET/PVC Samples

The surfaces of the GF/PTFE and PET/PVC samples were found to be hydrophobic, so the samples had to be chemically treated to improve their hydrophilicity and adhesion

properties. The type of polymer, treatment time and temperature affect the process results, such as roughness parameters, etching depth, and appearance of hydrophilic groups, so it is important to select the appropriate etching solution and optimum etching conditions. In order to improve the etching results prior to the treatment, the GF/PTFE and PET/PVC samples were mechanically ground with SiO<sub>2</sub> paper (p80 and p180 grit). The samples were then washed with hot running water and then with distilled water. This removed any dirt, dust, abrasive and broken particles adhering to the surface.

A thermo-oxidative acid treatment was chosen based on a literature analysis and our experience [36]. The composition of the etching solution and the etching conditions are given in Table 2.

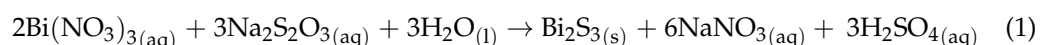
**Table 2.** Parameters of thermo-oxidative acid treatment of GF/PTFE and PET/PVC samples.

Solution Composition and Concentration, M	Sample	Etching Conditions	
		Temperature, °C	Duration, h
H <sub>2</sub> SO <sub>4</sub> , 7.2	GF/PTFE	100 ± 1	2
H <sub>3</sub> PO <sub>4</sub> , 6.6			
CrO <sub>3</sub> , 0.36	PET/PVC	68 ± 1	2

Although the GF/PTFE fabric is heat-resistant up to 260 °C, an etching process at around 100 °C was chosen to reduce the overall risk of the process. The PET/PVC fabric was heat-resistant to 70 °C, so the treatment was carried out at around 68 °C. Experiments were performed to determine the treatment time. At the end of the thermochemical treatment, the substrates were washed with hot running water, then rinsed with distilled water until the pH of the water reached a value of 7, and then air-dried at room temperature. The samples were then stored in a desiccator containing CaCl<sub>2</sub>.

### 2.3. Deposition of the Bi<sub>2</sub>S<sub>3</sub> Thin Films

The bismuth sulphide films were deposited using the SILAR method, which makes our technology simpler and cheaper. A series of experiments was carried out to investigate the effect of solution concentration, immersion time and number of cycles on the quality of the films. Solutions with a concentration of 0.02–0.1 M were investigated. The number of deposition cycles apparently has the greatest effect on film thickness, so for thin film deposition, immersion cycles were varied from 1 to 7. Finally, the samples were alternately immersed in solutions of 0.1 M Bi(NO<sub>3</sub>)<sub>3</sub> and 0.1 M Na<sub>2</sub>S<sub>2</sub>O<sub>3</sub> at room temperature and left undisturbed for 8 h. After each immersion in the solution, the samples were washed with distilled water. This constituted one deposition cycle. The number of immersion cycles seemed to have the greatest effect on the film thickness, so the immersion cycles were varied. The uniformity of the deposited film and the quality of its adhesion were checked visually and with a strong jet of water. The highest quality and best adhesion of Bi<sub>2</sub>S<sub>3</sub> films to the structural textile surface was achieved after seven cycles. The basic equation of the reaction can be described as follows:



After 7 deposition cycles, the colour of the samples changed; they became grey-black or black, and were covered with a visually uniform layer of deposited material.

### 2.4. Analytical Techniques

The changes in chemical structure and bond configuration on the surface of untreated and treated GF/PTFE and PET/PVC samples were analysed using attenuated total re-

flectance (ATR) Fourier-transform infrared (FTIR) spectroscopy. ATR-FTIR spectra were recorded in the wavenumber range of 3500–600  $\text{cm}^{-1}$ . Spectra were recorded on a Perkin Elmer FTIR Spectrum GX spectrophotometer by averaging 64 scans with a wavenumber resolution of 1  $\text{cm}^{-1}$  at room temperature.

X-ray diffraction (XRD) analysis was carried out on a Bruker Advance D8 diffractometer with a tube voltage of 40 kV and a tube emission current of 40 mA. The X-ray beam was filtered with a Ni 0.02 mm filter to select  $\text{CuK}\alpha$  ( $\lambda = 0.15406$  nm) radiation. Diffraction patterns were recorded in a Bragg–Brentano geometry by using a fast-counting detector, Bruker LynxEye, based on the silicon strip technology. The specimens of the samples were scanned over the range of  $2\theta = 3\text{--}70^\circ$  at a scan rate of  $0.02^\circ \text{min}^{-1}$  by using the coupled two theta/theta scan type.

The morphology and elemental analysis were investigated by scanning electron microscopy equipped with an energy dispersive X-ray spectroscopy detector (SEM-EDX). For SEM images, the samples were cut into smaller sizes of approximately  $5 \times 5$  mm and coated with gold (Au) prior to morphological observation. SEM, observation of the samples was performed on a ZEISS EVO MA10 microscope at an accelerating voltage of 20 kV. The Bruker AXSX Flash 6/10 detector can detect all the elements present in the sample with an overall accuracy of about 1% and a detection sensitivity down to 0.1% by weight. A Lambda 35 UV-Vis spectrophotometer was used to record the UV-Vis diffuse reflectance spectra of the structural textile and the resulting composites in the 200–800 nm spectral range. Barium sulphate was used as a white standard. The Kubelka–Munk method was used to determine the optical energy gap ( $E_g$ ) from the UV-Vis diffuse reflectance spectrum using the following equations [37,38]:

$$F(R) = \frac{(1 - R)^2}{2 \cdot R}, \quad (2)$$

$$h\nu F \sim (h\nu - E_g)^n, \quad (3)$$

where  $F$  is the Kubelka–Munk function,  $R$  is the reflectance,  $h\nu$  is the photon energy, and  $E_g$  is the optical energy gap,  $n$  is a constant denoting the power factor of the transition mode. For the allowed direct and indirect transitions,  $n = 2$  and  $1/2$ , respectively.

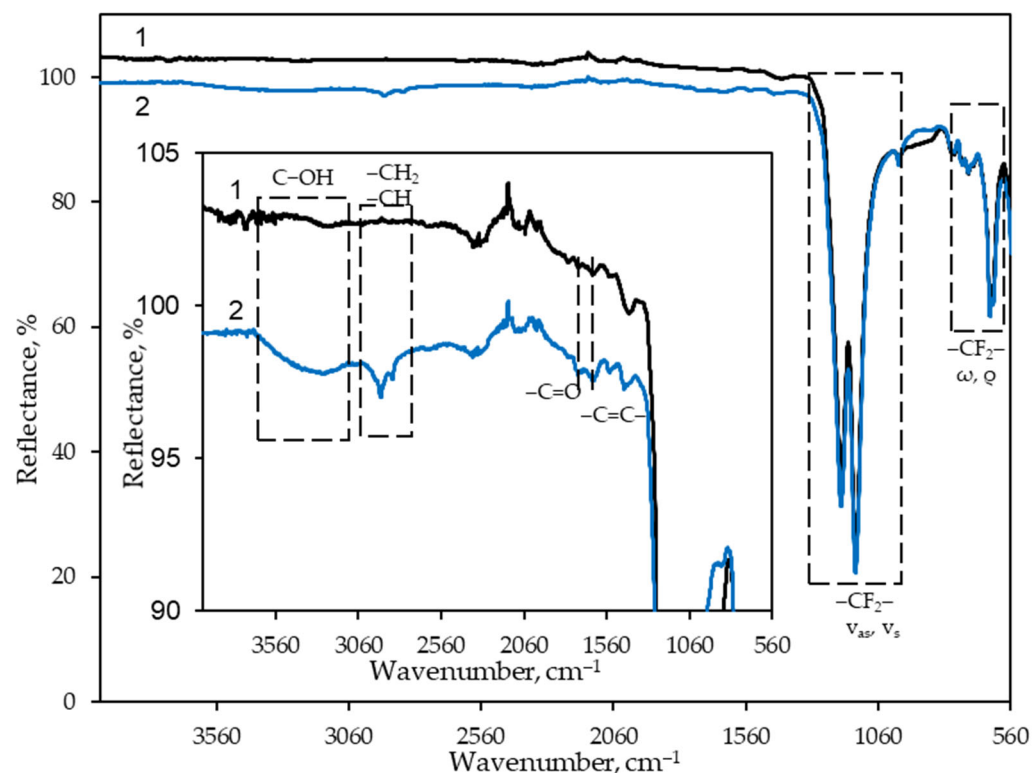
### 3. Results and Discussion

#### 3.1. ATR-FTIR Spectroscopy of GF/PTFE and PET/PVC Samples

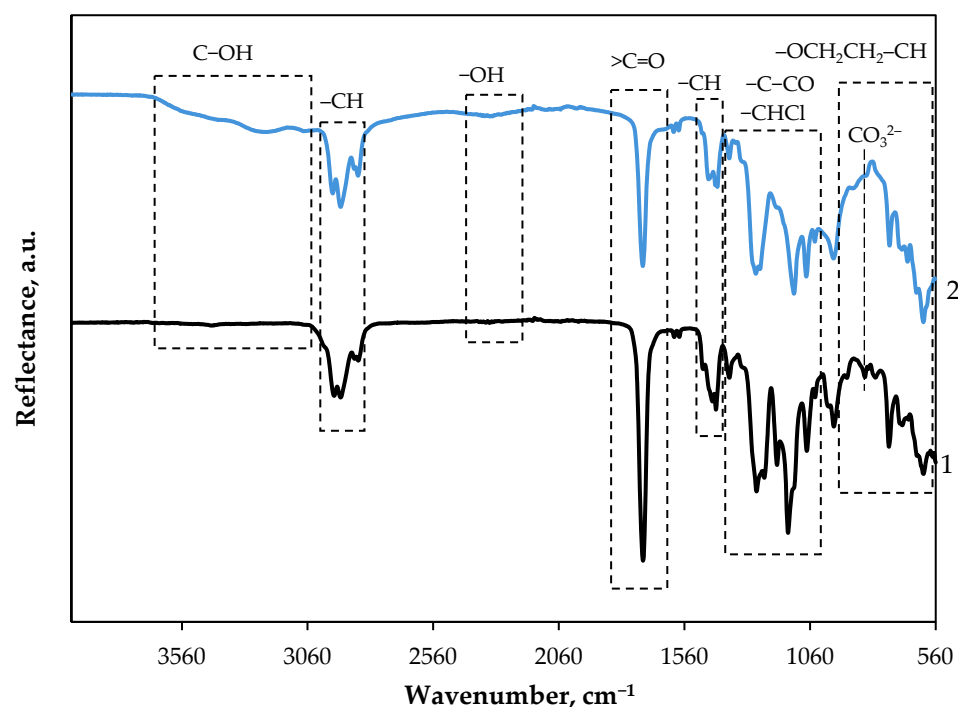
To better understand the changes in surface functional groups before and after chemical etching, the samples were analysed by ATR-FTIR spectroscopy. Figures 1 and 2 show the ATR-FTIR spectra of the untreated and etched GF/PTFE and PET/PVC samples.

Figure 1 illustrates the ATR-FTIR spectra of the GF/PTFE samples before and after etching. According to the literature [39], the most intense bands observed at 1145  $\text{cm}^{-1}$  and 1203  $\text{cm}^{-1}$  correspond to strong absorption of the valence symmetric and asymmetric stretching of  $\text{CF}_2$ , while the C–C vibration band appears as a curvature around 1250  $\text{cm}^{-1}$ . The peaks observed at 640  $\text{cm}^{-1}$ , 553  $\text{cm}^{-1}$ , and 507  $\text{cm}^{-1}$  correspond to  $\text{CF}_2$  deformation,  $\text{CF}_2$  wagging, and  $\text{CF}_2$  twisting, respectively, and undergo intense changes simultaneously with the degree of crystallinity of PTFE [40]. The strong peaks at 1093 and 798  $\text{cm}^{-1}$  are associated with asymmetric and symmetric Si–O–Si stretching vibrational bonding of glass fibre fabric [41]. However, the characteristic peak at 1093  $\text{cm}^{-1}$  of the Si–O–Si band is in the same region as the stretching of  $\text{CF}_2$ , resulting in an overlap of the peaks.





**Figure 1.** ATR-FTIR spectra of GF/PTFE architectural textiles in the 4000–560  $\text{cm}^{-1}$  wavenumber range: (1) untreated, (2) etched. The inset shows a magnified view of the x-axis.



**Figure 2.** ATR-FTIR spectra of PET/PVC structural textiles in the 4000–560  $\text{cm}^{-1}$  wavenumber range: (1) untreated; (2) etched.

To understand structural changes in the etched surface, the x-axis was magnified (Figure 1, inset). New functional groups appear in the ATR-FTIR reflectance spectrum of the etched GF/PTFE sample surface (inset in Figure 1, spectrum 2). The peak at 3675  $\text{cm}^{-1}$  is attributed to the valence vibrations of the -OH bond. The observed peaks at 2998  $\text{cm}^{-1}$ , 2900  $\text{cm}^{-1}$  and 1409  $\text{cm}^{-1}$  are assigned to valence asymmetric and valence symmetric C-H

and valence C=C bond vibrations, respectively. The unsaturated vibration of the C-F bond is fixed at  $925\text{ cm}^{-1}$ .

Figure 2 shows the ATR-FTIR spectra of an untreated and an etched PET/PVC sample surface. The coexistence of different types of functional groups in PET/PVC has a combined effect and, as a result, the positions of the infrared absorption peaks are different from those reported in the published data for the pure form. The ester group in PET/PVC textile is confirmed by an intense  $\text{>C=O}$  stretching vibration mode at  $1725\text{ cm}^{-1}$ , stretching vibrations of C=O bond at  $1192\text{ cm}^{-1}$ , a band at  $1148\text{ cm}^{-1}$  corresponding to asymmetric stretching vibrations of O-C-C group and a very weak absorption peak at  $1040\text{ cm}^{-1}$  resulting from C-O-C stretching vibrations [42–44]. The group of small vibrations in the spectral region from  $2950\text{ cm}^{-1}$  to  $2860\text{ cm}^{-1}$  could be attributed to the superposition of C-H stretching vibrations of  $\text{-CHCl}$ ,  $\text{CH}_3$ , and  $\text{-CH}_2$  groups of esters and  $\text{-CH}_2$  groups in PVC. The C-H wagging and rocking vibrations of the methylene groups are reflected in the bands at  $1435\text{ cm}^{-1}$  and  $965\text{ cm}^{-1}$ , respectively. The bands associated with the  $\text{-CHCl}$  functional group appear at  $1380\text{ cm}^{-1}$ ,  $1073\text{ cm}^{-1}$ , and  $693\text{ cm}^{-1}$  and correspond to the stretching vibrations of C-H, the skeletal vibration of  $\text{-CHCl}$ , and the stretching vibrations of C-Cl, respectively. The appearance of an intense peak at  $1274\text{ cm}^{-1}$  can be related to the complex superposition of three vibrations, such as C-H wagging in methylene groups of PVC chain, C-H bending vibrations of  $\text{-CHCl}$  moieties, and C=O stretching vibrations of ester group. This peak is observed at higher wavenumbers compared to the spectral position of the three peaks discussed above in pure PVC and the ester group of PET. Two weak absorption peaks at  $1600\text{ cm}^{-1}$  and  $1580\text{ cm}^{-1}$  are related to  $\text{-C=C}$  bond vibrations, while C-H out-of-plane bending vibrations of benzene rings are represented by peaks at  $877\text{ cm}^{-1}$ ,  $799\text{ cm}^{-1}$ , and  $745\text{ cm}^{-1}$  [42,45]. The minor peak at  $841\text{ cm}^{-1}$  can be attributed to  $\text{CaCO}_3$  acting as a filler [46]. As shown (Figure 2, spectrum 2), slight changes were observed in the ATR-FTIR spectra of the etched sample. All the peaks described for the untreated PET/PVC surface are slightly diminished or shifted. The minor peak attributed to  $\text{CO}_3^{2-}$  disappears, while  $\text{CaCO}_3$  dissolves in an acidic medium. The appearance of the broad band in the region from  $3656\text{ cm}^{-1}$  to  $3075\text{ cm}^{-1}$ , accompanied by a small shoulder in the region from  $2443\text{ cm}^{-1}$  to  $2194\text{ cm}^{-1}$ , confirms the formation of new  $\text{-OH}$  and/or  $\text{-C-OH}$  functional groups on the etched PET/PVC textile surface.

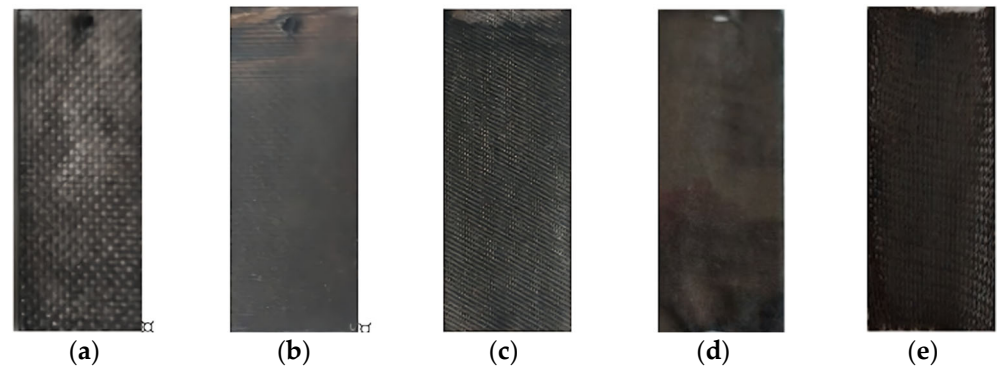
The ATR-FTIR spectra show a functionalised surface of GF/PTFE and PET/PVC samples after thermo-oxidative acid treatment with oxygen containing  $\text{>C=O}$  and  $\text{-C-OH}$  functional groups. The reactivity of the surface with these groups is much higher, while its hydrophilicity, and consequently the adhesion of deposited thin  $\text{Bi}_2\text{S}_3$  semiconductor films, is increased.

### 3.2. Structural, Morphological and Optical Characterisation of Obtained Composites

A visual evaluation of the surface of the resulting composites revealed a significant colour change to dark brown or black, confirming the formation of a new phase on the surface of the textile samples (Figure 3).

The deposited films were tested for adhesion by subjecting them to a steady stream of distilled water [47]. The tests show that deposited thin films adhered well to the textile substrates.

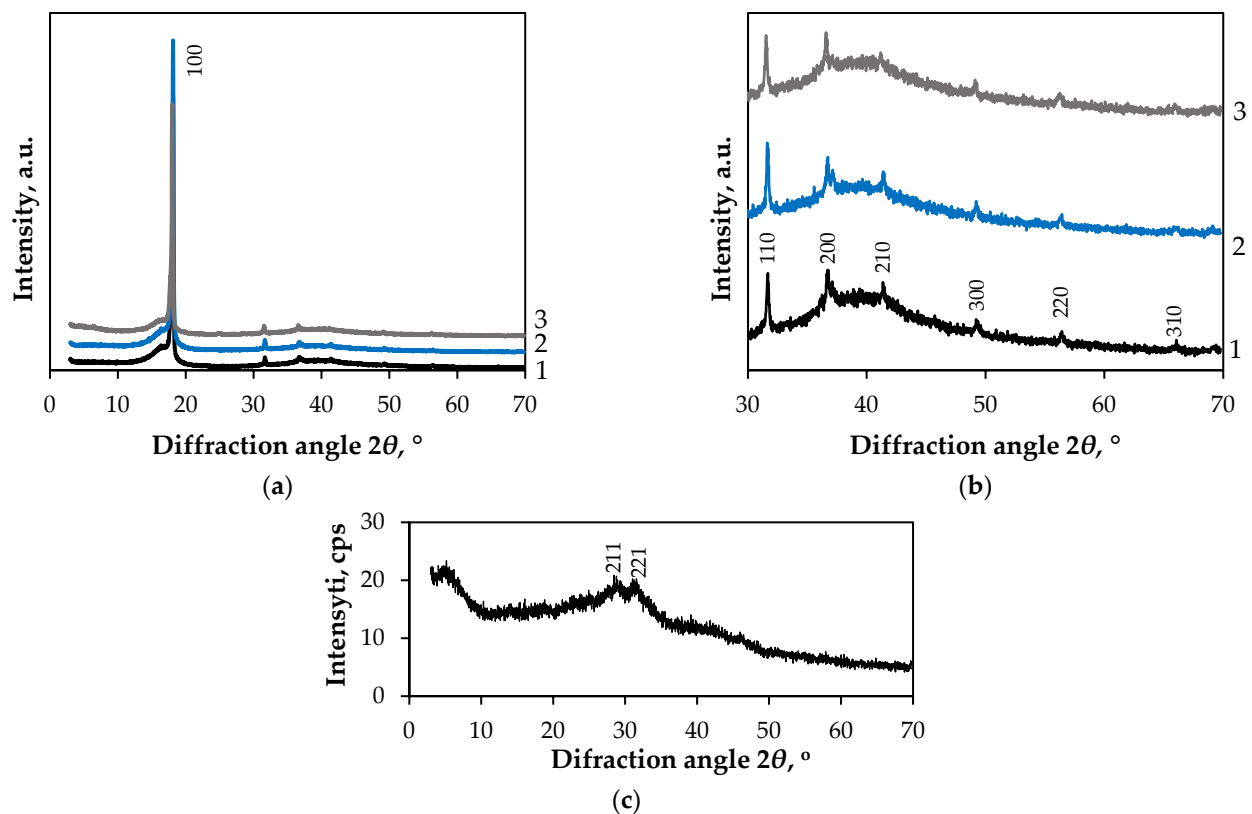
XRD was used to characterise the phase composition of the  $\text{Bi}_2\text{S}_3$  thin films obtained. SEM-EDX spectroscopy was used to evaluate the surface morphology and elemental composition. UV-Vis DR spectroscopy indirectly measures the electronic structure of a solid to provide information about the electronic transitions of its different orbitals [38], and is the most effective method for evaluating the optical properties of textile fibres [48].



**Figure 3.** Images of obtained composites: (a) GF/PTFE/Bi-S; (b) PET/PVC/Bi-S; (c) C/PES/S/Bi-S; (d) PA/Cu/Bi-S; (e) PA/Ag/Bi-S.

### 3.2.1. Characterisation of GF/PTFE/Bi-S Samples

XRD analysis was performed to better understand the changes in the surface phase composition of the untreated and etched GF/PTFE samples, as well as the GF/PTFE/Bi-S composite. XRD diffractograms are shown in Figure 4. The XRD data was analysed in detail using a combination of data from the literature and JCPDS reference templates.



**Figure 4.** XRD diffractogram of (1) untreated GF/PTFE sample; (2) etched GF/PTFE sample; (3) GF/PTFE/Bi-S composite. (a) Full range; (b) zoomed-in view between 30 and 70  $2\theta$ ; (c) scraping from a GF/PTFE/Bi-S composite surface.

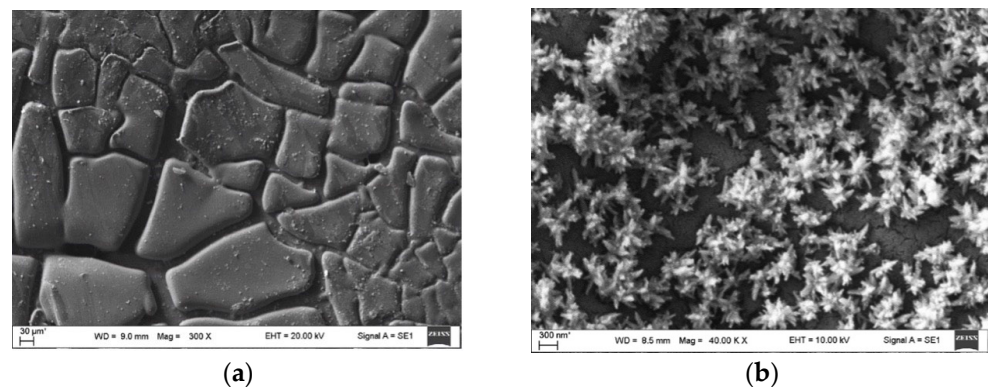
According to the literature [49], PTFE is characterised by one intense X-ray diffraction peak at  $2\theta = 18^\circ$  and six peaks of low intensity appearing at  $2\theta = 30^\circ$  to  $70^\circ$ . These peaks correspond to (100), (110), (200), (210), (300), (220), and (310) crystal planes. Analysing the obtained XRD data of the untreated GF/PTFE construction textile sample (Figure 4, diffractogram 1), the diffraction peaks at  $2\theta = 18.05^\circ, 31.66^\circ, 36.88^\circ, 41.40^\circ, 49.32^\circ, 56.48^\circ$ ,



and  $66.10^\circ$  were recorded in the specified interval, which are attributed to crystalline PTFE (JCPDS: 47-2217).

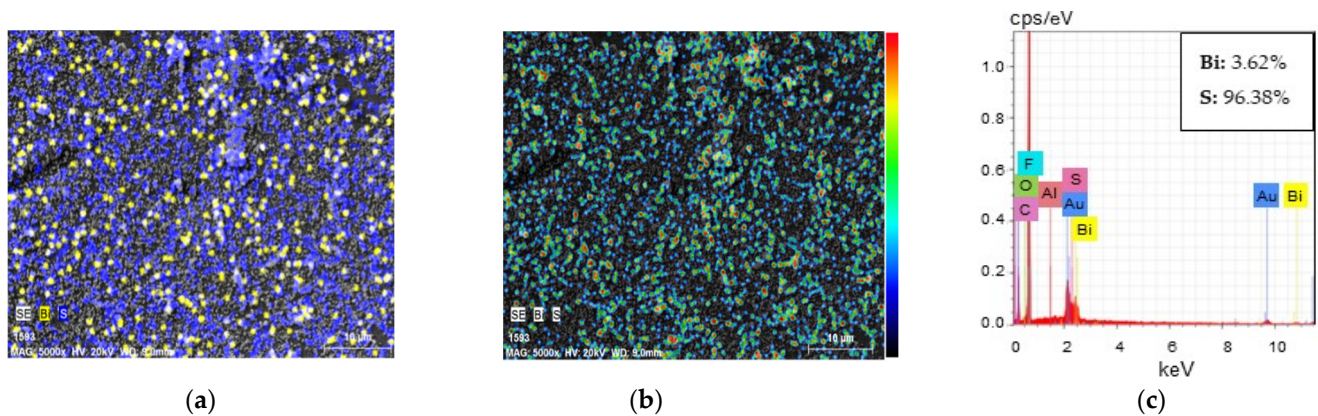
After etching, no significant changes were observed in the position of any of the characteristic peaks of untreated GF/PTFE ( $2\theta = 18.09^\circ, 31.65^\circ, 36.82^\circ, 41.40^\circ, 49.27^\circ, 56.35^\circ$ , and  $66.10^\circ$ , Figure 4, diffractogram 2), although the intensity of the peaks at  $2\theta = 18.09^\circ$  and  $31.65^\circ$  increased. No new peaks appeared. A sharp increase in the intensity of the peak indicates both an increase in the size of the crystallites and their preferred orientation. The grain size, calculated using XRD patterns according to Debye–Scherer’s formula [50], is 23.72 nm for the untreated GF/PTFE textile samples at the (100) crystal plane. For the etched samples, the grain size is 24.37 nm, i.e., it increases. Increasing the average grain size of a GF/PTFE surface decreases its available surface area for deposition. This can hinder chemical reactions and alter adhesion, resulting in a surface that is less uniform and reactive for thin film deposition. This is because larger grains create fewer nucleation sites, resulting in a rougher surface with more pronounced voids between particles that can trap reactants or hinder coverage.

A diffractogram similar to that of the etched GF/PTFE sample was obtained after  $\text{Bi}_2\text{S}_3$  thin films were deposited (see Figure 4, diffractogram 3). As previously reported [51], chemically deposited  $\text{Bi}_2\text{S}_3$  films are often amorphous or polycrystalline in their as-deposited state. SEM images (Figure 5b) show that the GF/PTFE surface is covered with nanostar-shaped crystallites that are characteristic of the  $\text{Bi}_2\text{S}_3$  nanostructure. Therefore, we scraped a deposited layer from a composite surface and analysed it using XRD. The presence of XRD peaks at  $2\theta = 28.45^\circ$  and  $31.57^\circ$  in the scraped material indicates that it is polycrystalline (see Figure 4c). These peaks are attributed to the orthorhombic phase of  $\text{Bi}_2\text{S}_3$ , with the following crystallographic planes: (211) and (221) (JCPDS: 17-320). EDX spectra (Figure 6c) showed that the deposited film was rich in sulphur. However, no sulphur peaks were registered. These results lead us to conclude that the deposited film is much thinner than the substrate, so no new phases could be detected in the diffractogram.



**Figure 5.** SEM images of GF/PTFE/Bi-S composite: (a) 300 $\times$  magnified; (b) 40,000 $\times$  magnified.

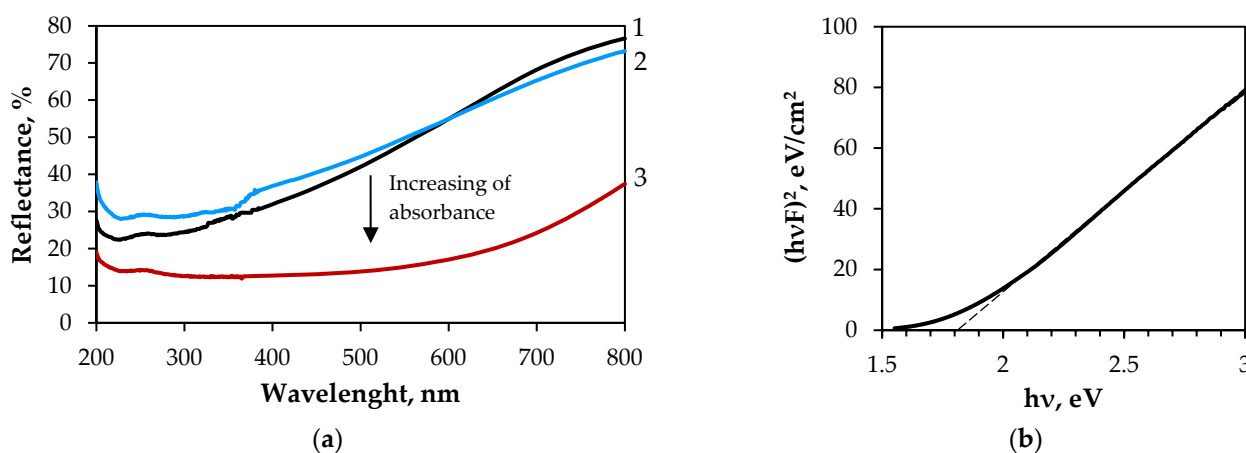
Figure 5 shows SEM images of the GF/PTFE/Bi-S composite. Figure 5a shows that the surface is uneven, with cracks separating smooth clusters of various sizes. Increased magnification (Figure 5b) reveals nanostar-shaped structures on the substrate surface, which are characteristic of the  $\text{Bi}_2\text{S}_3$  nanostructure. The nanostar particles and their aggregates vary significantly in size, ranging from approximately 300 nm to around 1.2  $\mu\text{m}$ .



**Figure 6.** EDX elemental maps of Bi (yellow) and sulphur (blue) ( $10,000\times$  magnified) of GF/PTFE/Bi-S surface: (a) spatial distribution of elements; (b) elemental concentration distribution; (c) representative EDX spectra. The normalised atomic percentages of Bi and S in the films are shown in the corresponding inset.

The elemental distribution was analysed using energy dispersive X-ray spectroscopy (EDX). Spatial and concentration distributions of bismuth and sulphur on GF/PTFE are shown in Figure 6. Spatial distribution shows a clustered distribution of both elements. Yellow spots (bismuth) appear to form dense clusters; brighter white spots correspond to nanostar-shaped  $\text{Bi}_2\text{S}_3$  structures visible in SEM analysis. Blue matrix (sulphur) surrounds these clusters, suggesting sulphur is more evenly distributed over the substrate. Image B shows small yellow-green spots scattered across a darker background, confirming localised enrichment of certain elements. The surface shows heterogeneous concentration distribution, reinforcing the idea of nanostar-structured deposition rather than a uniform layer. As can be seen from the representative EDX spectra presented in Figure 6c, the Bi and S peaks are clearly visible in the EDX spectra of the samples, alongside additional peaks due to the GF/PTFE substrate, the substrate holder used in the EDX instrument, or the Au coating applied prior to morphological observation. The inset in Figure 6c shows the normalised atomic percentages of bismuth and sulphur. The atomic ratios of Bi and S vary within the respective ranges of 3.62% and 96.38%. This indicates a high excess of sulphur. The excess S in  $\text{Bi}_2\text{S}_3$  films prepared using  $\text{Na}_2\text{S}_2\text{O}_3$  may also be due to thiosulphate, since thiosulphate can decompose into elemental S in an acidic medium [52]. This acidic medium is formed during the hydrolysis of  $\text{Bi}(\text{NO}_3)_3$ .

Figure 7a shows the reflectance values of the untreated and etched GF/PTFE textile and GF/PTFE/Bi-S composite in the UV–Vis region. PTFE, a key component of the textile, has an average reflectance of over 93% from 250 to 400 nm, reaching around 99% in the visible and near-infrared spectrum [53]. However, its high diffuse reflection decreases with increasing GF content in textiles. For the untreated GF/PTFE textile, the percentage reflectance increases gradually from 25% at 200 nm to 76% at 800 nm (Figure 7a, spectrum 1), whereas for the etched textile, it increases gradually from 32% at 200 nm to 73% at the same wavelength (Figure 7a, spectrum 2). Depositing  $\text{Bi}_2\text{S}_3$  films influences the reflectance of the GF/PTFE/Bi-S composite. Reflectance plateaus at around 13% between 200 and 500 nm before steadily increasing to 36% at 800 nm (Figure 7a, spectrum 3).

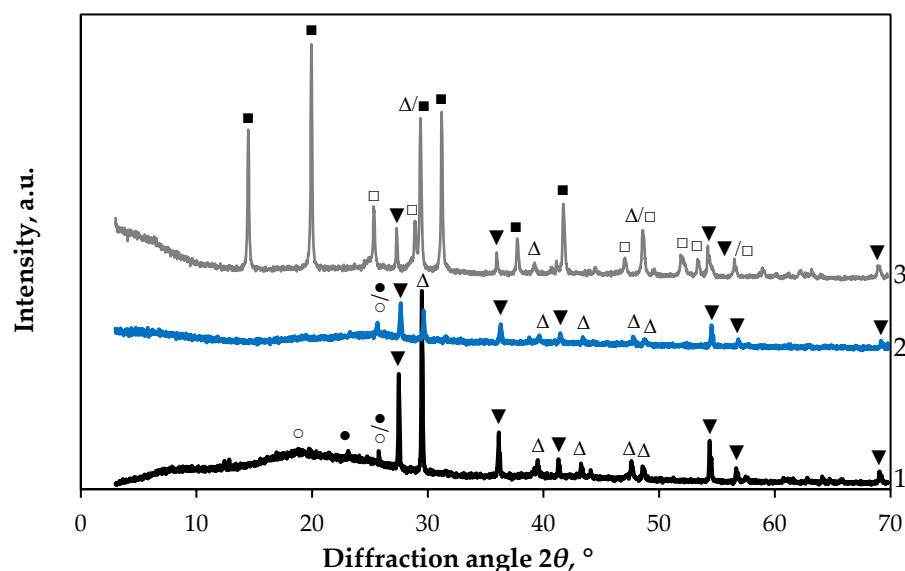


**Figure 7.** (a) Optical reflectance spectra as a function of the wavelength in the range of 200–800 nm for (1) untreated GF/PTFE; (2) etched GF/PTFE; (3) GF/PTFE/Bi-S composite; (b)  $E_g$  determination by Kubelka–Munk method.

The  $E_g$  value was determined from the UV-Vis DR spectrum by applying the Kubelka–Munk method. The experimental data show a long straight-line section in the  $(h\nu F)^2$  vs.  $h\nu$  chart (Figure 7b), whereas the  $(h\nu F)^{1/2}$  vs.  $h\nu$  plots exhibit no linear behaviour, ruling out the possibility of an indirect optical energy gap. The intersection between the linear fit and the photon energy axis gives an  $E_g$  value of 1.8 eV (Figure 7b).

### 3.2.2. Characterisation of PET/PVC/Bi-S Samples

The diffractogram patterns of the PET/PVC samples before and after thermochemical treatment, as well as the obtained composites, are shown in Figure 8. A combination of data from the literature and JCPDS reference templates was used to analyse the XRD data in detail.



**Figure 8.** XRD diffractogram of (1) untreated PET/PVC sample; (2) etched PET/PVC sample; (3) PET/PVC/Bi-S composite. Peaks are labelled as follows: ●—PET (JCPDS: 50-2275); ○—PVC (JCPDS: 64-1628); Δ—rhombohedral CaCO<sub>3</sub> (JCPDS: 05-0586); ▼—tetragonal TiO<sub>2</sub> (JCPDS: 04-006-1890); □—orthorhombic Bi<sub>2</sub>S<sub>3</sub> (JCPDS: 17-320); ■—monoclinic S (JCPDS: 76-183).

The XRD diffractogram of the untreated sample (Figure 8, curve 1) shows a broad, weak characteristic peak of PVC at  $2\theta = 18.78^\circ$ , corresponding to the (110) crystal plane

(JCPDS: 64-1628). The PET peak is observed at  $2\theta = 23.07^\circ$  (JCPDS: 50-2275), and the peak at  $2\theta = 25.78^\circ$  can be attributed to both PET and PVC. The five characteristic peaks at  $2\theta = 29.49^\circ$ ,  $39.49^\circ$ ,  $43.38^\circ$ ,  $47.69^\circ$ , and  $48.63^\circ$  correspond to the (104), (113), (202), (016), and (018) crystal planes of rhombohedral calcite ( $\text{CaCO}_3$ , JCPDS: 05-0586). Similarly, six characteristic peaks at  $2\theta = 27.50^\circ$ ,  $36.14^\circ$ ,  $41.28^\circ$ ,  $54.38^\circ$ ,  $56.83^\circ$ , and  $69.23^\circ$  correspond to the (110), (101), (200), (211), (220), and (301) crystal planes of the tetragonal rutile phase of titanium dioxide ( $\text{TiO}_2$ ; JCPDS: 04-006-1890).

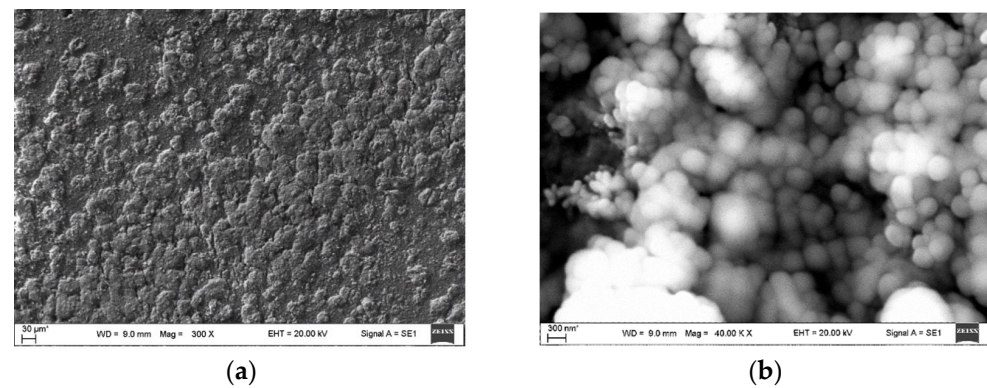
In general, no phase changes occur after thermochemical treatment. However, there is a clear variation in the diffraction peaks corresponding to the peaks of both the organic components and the inorganic filler (Figure 8, diffractogram 2). The broad, weak PVC characteristic peak at  $2\theta = 18.78^\circ$  and the small PET peak at  $2\theta = 23.07^\circ$  disappear. Following treatment, the intensity of all  $\text{TiO}_2$  peaks decreases compared to the untreated sample, as do those corresponding to  $\text{CaCO}_3$ . This suggests that the crystalline quality of the inorganic fillers has been reduced. A decrease in the intensity of all XRD peaks in a sample compared to an untreated sample suggests a change in the material's crystallinity or composition. As no new phase was identified, this could be due to factors such as reduced crystal size, increased lattice strain or an increased concentration of amorphous phases. The reduced crystallinity of the samples appeared to hinder fibre agglomeration and facilitate the diffusion of precursor ions.

After the deposition of thin films, a series of new peaks appear (see Figure 8, diffractogram 3). As reported [54], prominent  $2\theta$  peaks for orthorhombic phase bismuthinite ( $\text{Bi}_2\text{S}_3$ ) in XRD patterns are typically found at around  $28.6^\circ$  and  $31.8^\circ$ . However, the specific  $2\theta$  values and their corresponding intensities may differ slightly depending on the synthesis method used and the quality of the  $\text{Bi}_2\text{S}_3$  crystal. Therefore, the peak at  $2\theta = 28.67^\circ$  (211) is attributed to the orthorhombic phase of  $\text{Bi}_2\text{S}_3$  (JCPDS: 17-320). Additional  $\text{Bi}_2\text{S}_3$  peaks may be observed at  $2\theta = 25.32^\circ$  (310),  $47.05^\circ$  (350),  $52.02^\circ$  (540), and  $53.37^\circ$  (061). The increased intensity of the peak at around  $2\theta = 48.63^\circ$ , initially attributed to calcite, shows that it overlaps with an additional  $\text{Bi}_2\text{S}_3$  peak at  $2\theta = 48.62^\circ$  (060). Similarly, the increased intensity of the peak at around  $2\theta = 56.83^\circ$ , initially attributed to rutile, shows that it overlaps with an additional  $\text{Bi}_2\text{S}_3$  peak at  $2\theta = 56.53^\circ$  (451). Peaks at  $2\theta$  values of  $14.48^\circ$  (210),  $19.94^\circ$  (120),  $31.22^\circ$  ( $-601$ ),  $37.76^\circ$  (133), and  $41.76^\circ$  ( $-721$ ) can be assigned to monoclinic sulphur (JCPDS 76-183). Similarly, to  $\text{Bi}_2\text{S}_3$ , the increased intensity of the peak at around  $2\theta = 29.49^\circ$ , initially attributed to calcite, shows that it overlaps with an additional sulphur peak at  $2\theta = 29.32^\circ$  (420).

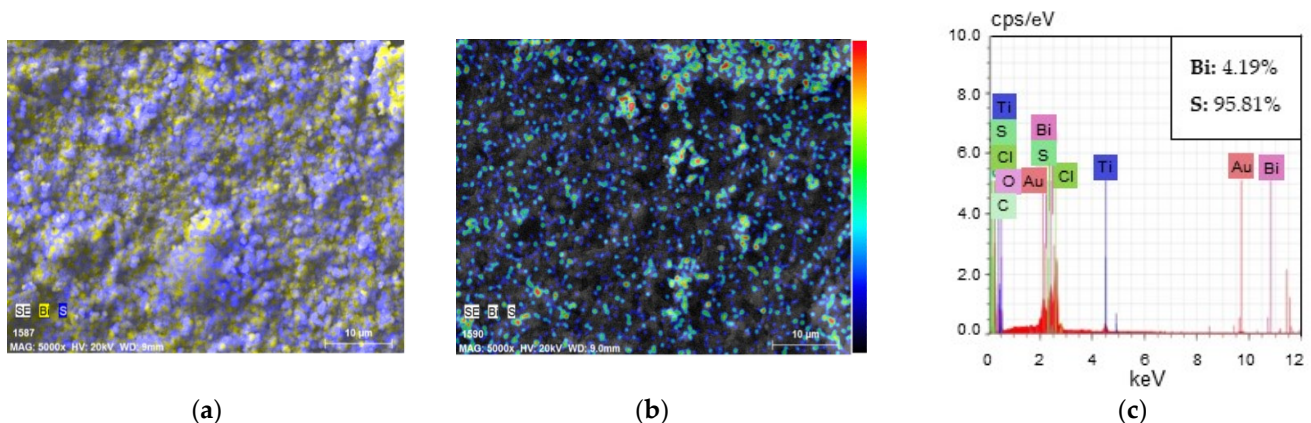
Figure 9 shows SEM images of the deposited  $\text{Bi}_2\text{S}_3$  thin film onto PET/PVC. From image Figure 9a, it is concluded that the surface is even; no cracks or pores are visible. Higher magnification (Figure 9b) shows uniform nanosphere-shaped structures that differ in size (individual spheres measuring 100 nm and agglomerates measuring  $1.14\text{ }\mu\text{m}$ ), with no gaps separating them. It can be speculated that the films grew by forming separate groups of nanoparticles in specific locations, gradually covering the entire textile surface with each subsequent deposition cycle.

Elemental distribution was analysed using EDX. Spatial and concentration distributions of bismuth and sulphur on PET/PVC are shown in Figure 10. The distribution of Bi and S appears relatively uniform. There are no large agglomerations of Bi or S; the two elements seem co-localised throughout the surface of the substrate, although sulphur seems to be more evenly spread out across the surface. Results suggest a homogeneous composition, consistent with a well-formed composite. Image Figure 10b shows small yellow-green spots scattered across a darker background, confirming localised enrichment of certain elements. While concentration distribution is relatively even, higher concentration in certain areas suggests influxes that might be attributed to larger nanostructures.





**Figure 9.** SEM images of PET/PVC/Bi-S composite: (a) 300 $\times$  magnified; (b) 40,000 $\times$  magnified.



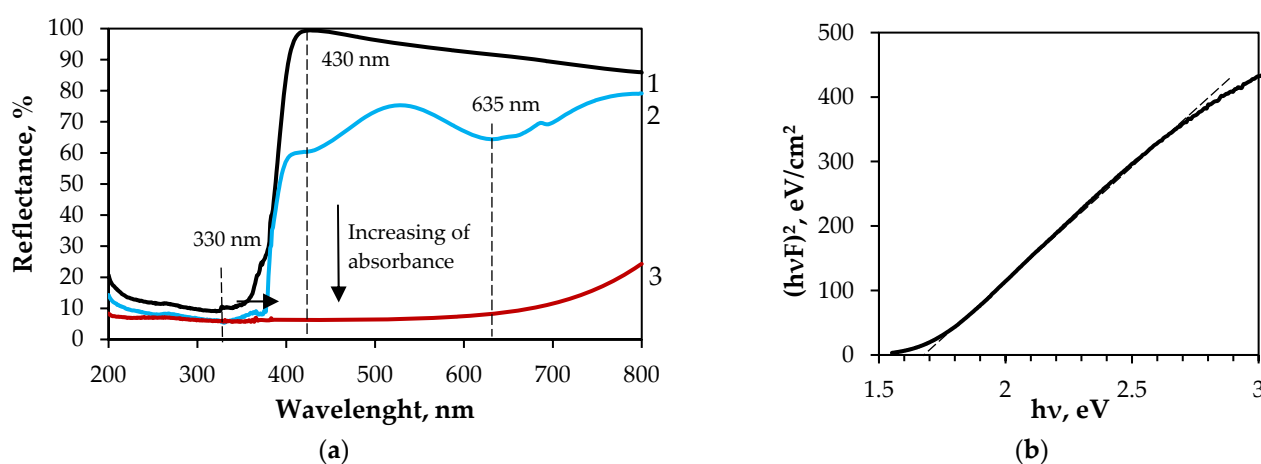
**Figure 10.** EDX elemental maps of Bi (yellow) and sulphur (blue) (10,000 $\times$  magnified) of PET/PVC/Bi-S surface: (a) spatial distribution of elements; (b) elemental concentration distribution; (c) representative EDX spectra. The normalised atomic percentages of Bi and S in the films are shown in the corresponding inset.

As can be seen from the results presented in Figure 10c, the Bi and S peaks are clearly visible in the EDX spectra of the samples, alongside additional peaks due to the PET/PVC substrate, its fillers, the substrate holder used in the EDX instrument or the Au coating applied prior to morphological observation. The inset in Figure 10c shows the normalised atomic percentages of bismuth and sulphur. The atomic ratios of Bi and S vary within the respective ranges of 4.19% and 95.81%. This indicates a high excess of sulphur, and the obtained results are in good agreement with XRD data.

Figure 11 shows the UV–Vis DR spectra of the untreated and etched PET/PVC samples, as well as the PET/PVC/Bi-S composite. PET fibres, which have a structure based on aromatic components, exhibit strong absorption of shorter ultraviolet wavelengths [55]. PVC is reported to exhibit absorption maxima at 280 and 245 nm in the UV region due to  $\pi$ – $\pi^*$  electronic transitions in the polymer backbone [56]. However, the PET/PVC textile used in this study exhibits a sharp absorption profile beyond 430 nm and minimal reflectance at 330 nm. This UV–Vis absorption profile is similar to that of  $\text{CaCO}_3/\text{TiO}_2$  hybrid particles [57], which are utilised commercially. XRD analysis has revealed that the PET/PVC textile contains well-dispersed microparticles of  $\text{CaCO}_3$  and  $\text{TiO}_2$  acting as fillers. The polymer industry commonly employs  $\text{TiO}_2$  in two capacities: as a white pigment and a UV-blocking additive. The primary function of these two applications is to prevent polymer degradation caused by UV exposure.  $\text{TiO}_2$  is also a photocatalyst, which makes it perfect for use in self-cleaning coatings on different materials [58]. The reflectance intensity of the untreated PET/PVC sample in the 200–360 nm range is about 10–20%. Then, at 360 nm, it increases sharply, reaching 100% at 430 nm. Reflectance then gradually decreases, reaching



86% at 800 nm (Figure 11, spectrum 1). In the spectrum of the etched PET/PVC sample (see Figure 11, spectrum 2), a red shift was observed in the region of high absorption up to 370 nm due to the incorporation of functional groups in the PVC matrix. Within the 200–370 nm spectral range, the reflectance intensity of the etched PET/PVC sample is around 7–13%. Then, from 370 to 430 nm, this value increases sharply to 60%, continuing to rise until it reaches a nearly constant value of around 75–79% at 800 nm. Two additional broad absorption peaks were observed at 430 and 635 nm, which are associated with the functionalised surface. Within the 200–635 nm wavelength range, the PET/PVC/Bi-S composite's reflectance reaches a value of around 7% (see Figure 11, spectrum 3). This then increases monotonically to 24% at 800 nm. This composite demonstrates very good sunlight absorption.



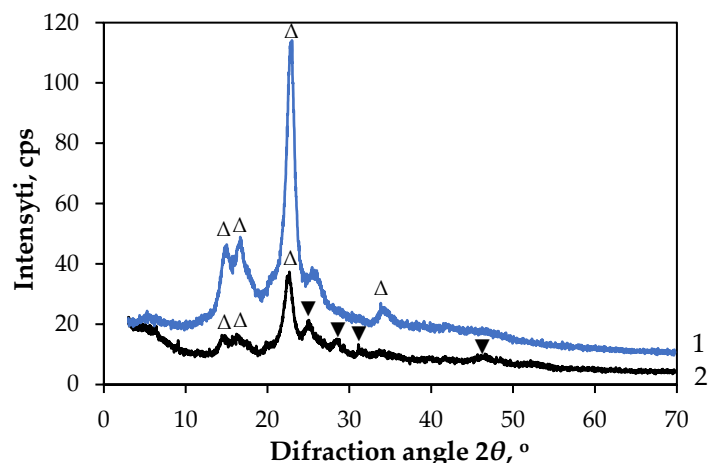
**Figure 11.** (a) Optical reflectance spectra as a function of the wavelength in the range of 200–800 nm for (1) untreated PET/PVC; (2) etched PET/PVC; (3) PET/PVC/Bi-S composite. Photograph of the PET/PVC/Bi-S sample shown in the inset; (b)  $E_g$  determination by Kubelka–Munk method.

An  $E_g$  value of 1.68 eV for the PET/PVC/Bi-S composite is given by the intersection between the linear fit and the photon energy axis (Figure 11b).

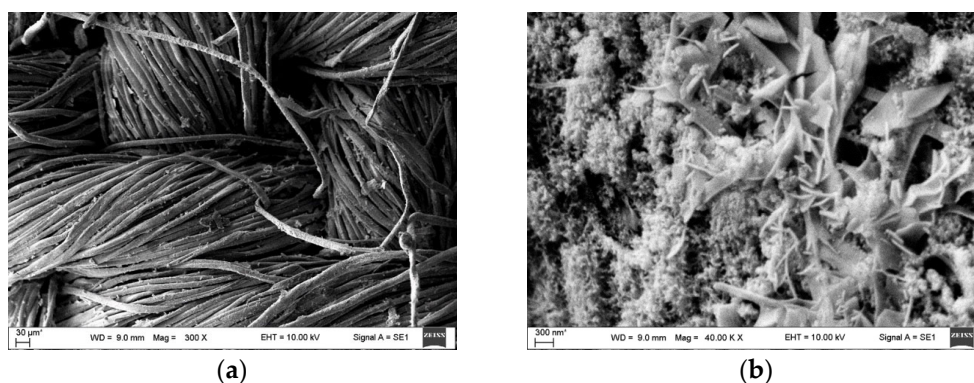
### 3.2.3. Characterisation of C/PES/S/Bi-S Samples

XRD was performed to obtain further information on the crystalline structure of the C/PES/S samples and the obtained composites (Figure 12). The XRD pattern of cellulose I, which is found within the cotton fibres, peaks are typically observed at the following  $2\theta$  angles:  $15.2^\circ$ ,  $16.7^\circ$ , and  $23.1^\circ$  (JCPDS: 03-0226). The diffraction patterns of the C/PES/S samples exhibited the peaks at  $2\theta = 15.01^\circ$ ,  $16.67^\circ$ ,  $22.99^\circ$ , and  $34.23^\circ$ , corresponding to the crystal lattice planes 110, 200, 220, and 004 of cellulose [54,59]. In the C/PES/S/Bi-S composite, the intensity of these peaks decreased and shifted to  $2\theta = 14.42^\circ$ ,  $16.20^\circ$ , and  $22.66^\circ$  compared to the initial sample. The peak at  $34.23^\circ$  disappeared. This suggests that the crystalline structure of cellulose changes after deposition of  $\text{Bi}_2\text{S}_3$  films. In addition, new peaks appeared at  $2\theta = 25.05^\circ$  (310),  $28.43^\circ$  (211),  $31.61^\circ$  (221), and  $46.57^\circ$  (501), which belong to the orthorhombic phase of  $\text{Bi}_2\text{S}_3$  (JCPDS: 17-320). No sulphur peaks were detected.

Figure 13 shows SEM images of deposited  $\text{Bi}_2\text{S}_3$  thin film onto C/PES/S. Image Figure 13a shows that the deposited  $\text{Bi}_2\text{S}_3$  coated the individual strands of material evenly. Figure 13b reveals an unorganised variety of differently shaped structures, including nanoflakes and nanoflowers. No cracks or pores are visible. The varying shapes are likely to have formed due to the uneven C/PES/S surface.



**Figure 12.** XRD diffractogram of samples: (1) C/PES/S; (2) C/PES/S/Bi-S. The peaks are labelled as follows:  $\Delta$ —cotton (JCPDS: 03-0226);  $\blacktriangledown$ —orthorhombic  $\text{Bi}_2\text{S}_3$  (JCPDS: 17-320).

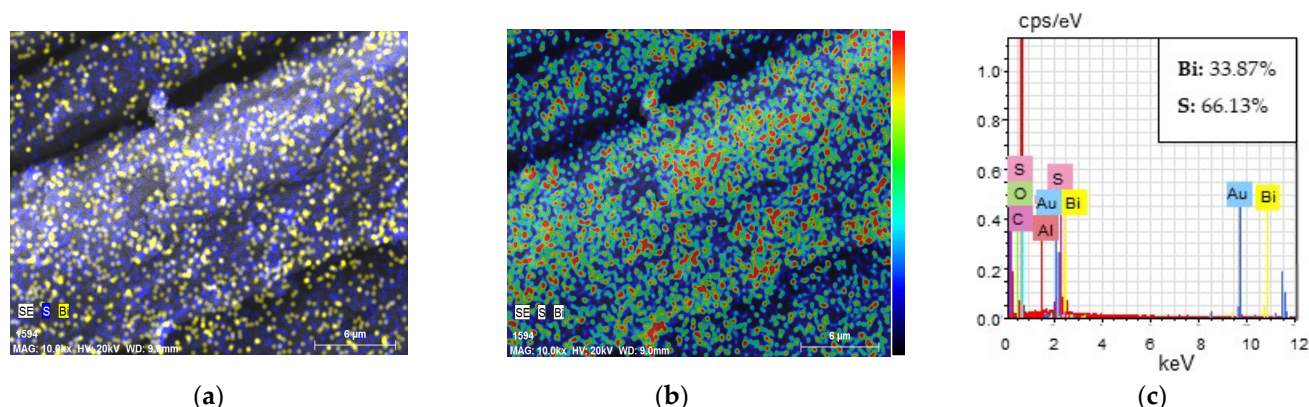


**Figure 13.** SEM images of C/PES/S/Bi-S composite: (a) 300 $\times$  magnified; (b) 40,000 $\times$  magnified.

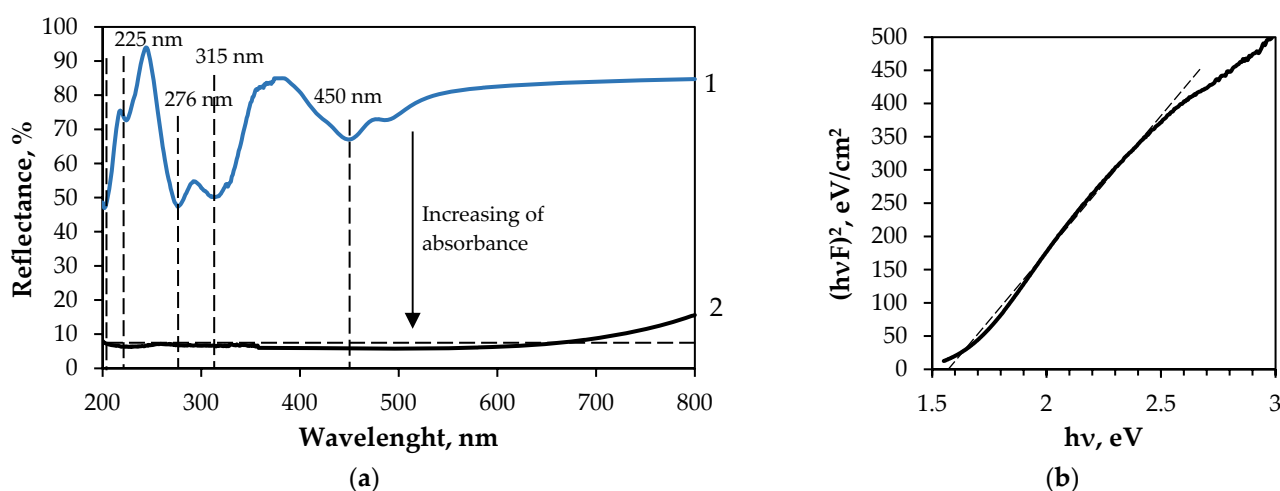
Spatial and concentration distributions of bismuth and sulphur on C/PES/S are shown in Figure 14. Spatial distribution (Figure 14a) shows an equal distribution of both bismuth and sulphur; no large clusters of either element are visible. Figure 14b shows a moderately large concentration of elements, which suggests large nanostructures with some lower concentration zones indicating smaller ones. These results confirm the formation of smaller nanoflakes and larger nanoflowers. As can be seen from Figure 14c, the EDX spectra of the samples clearly show peaks of bismuth (Bi) and sulphur (S), as well as additional peaks resulting from the substrate, the substrate holder used in the EDX instrument or the gold (Au) coating applied before morphological observation. The inset in Figure 14c shows the normalised atomic percentages of Bi and S. The atomic ratios of Bi and S vary within the respective ranges of 33.87% and 66.13%. The results obtained indicate a slight excess of amorphous sulphur (no S peaks were detected) and are in good agreement with the XRD data. It was reported [60,61] that atomic percentages of 40% Bi and 60% S in  $\text{Bi}_2\text{S}_3$  films indicate stoichiometry. This suggests that the films formed on the C/PES/S substrate have a bismuth-to-sulphur molar ratio approaching that of the  $\text{Bi}_2\text{S}_3$  compound.

Diffuse reflectance spectra were recorded to measure the amount of light reflected by a sample across the ultraviolet and visible light spectrums. Cotton generally reflects a significant portion of visible light. Its reflectance spectrum shows a gradual increase with increasing wavelength, reaching a plateau in the visible region. Its reflectance in the UV region (wavelengths below 400 nm) is particularly useful for distinguishing it from other textile fibres, such as viscose, bamboo, modal and Tencel, which tend to have a higher reflectance in this region [62]. The way light is reflected by cotton changes as its colour changes. In our study, the C/PES/S samples were coloured green/yellow. As these

samples are a blend of three types of material (cotton, polyester and spandex), their UV-Vis DRS spectra differ from those of pure cotton fibres (Figure 15a).



**Figure 14.** EDX elemental maps of Bi (yellow) and sulphur (blue) ( $10,000\times$  magnified) of C/PES/S/Bi-S surface: (a) spatial distribution of elements; (b) elemental concentration distribution; (c) representative EDX spectra. The normalised atomic percentages of Bi and S in the films are shown in the corresponding inset.

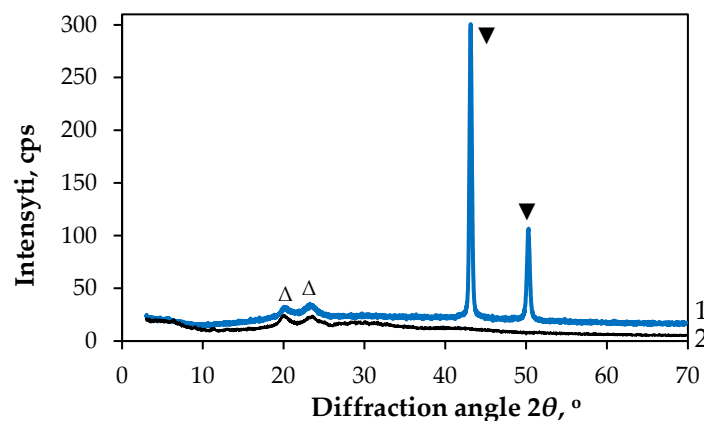


**Figure 15.** (a) Optical reflectance spectra as a function of the wavelength in the range of 200–800 nm for samples: (1) C/PES/S; (2) C/PES/S/Bi-S. Photograph of the C/PES/S/Bi-S sample shown in the inset; (b)  $E_g$  determination for C/PES/S/Bi-S by Kubelka–Munk method.

Typically, UV-Vis absorption spectra of cellulose I show minimal absorbance in the visible region (380–700 nm), with a decrease as the wavelength increases. A peak in the UV region, usually around 270–283 nm, is often associated with impurities such as lignin. Reflectance minima (peaks of absorbance) at around 200 and 225 nm are typical of  $\pi \rightarrow \pi^*$  electronic transitions in CC double bonds in polymer chains. Cotton fabrics have some disadvantages, such as low ultraviolet blocking [62]. Therefore, textiles are treated with a UV stabiliser. A peak at 310 nm could indicate the presence of a UV stabiliser, which typically has a peak in the range of 290–315 nm [63]. As shown in Figure 15a, spectrum 2, the absorption of samples increases after deposition of  $\text{Bi}_2\text{S}_3$  thin films, reaching about 92% in the ultraviolet and visible regions. The  $E_g$  value for the C/PES/S/Bi-S composite is 1.58 eV, as determined by the intersection of the linear fit and the photon energy axis (Figure 15b). The C/PES/S/Bi-S composite also demonstrates great potential for use as a solar cell absorber component.

### 3.2.4. Characterisation of PA/Cu/Bi-S Samples

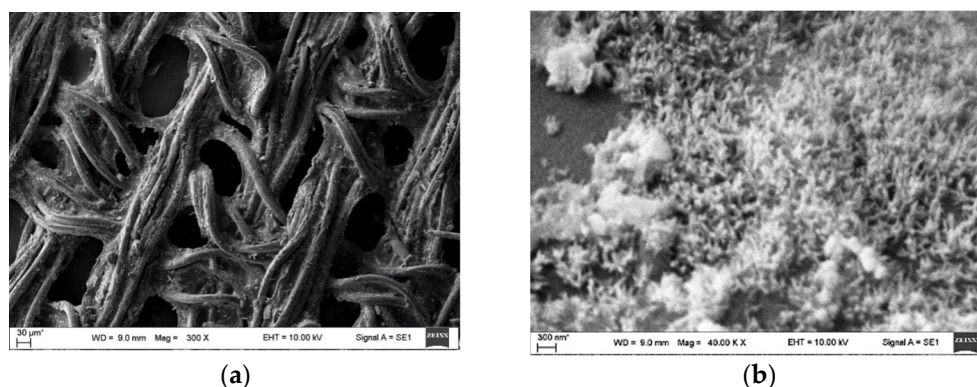
The PA/Cu textile under investigation was manufactured by depositing a layer of copper nanoparticles on the surface of the PA6 fibre fabric. The crystalline structure of the PA/Cu samples and the obtained composites was investigated using XRD (see Figure 16). The diffraction patterns of the PA/Cu samples (Figure 16, diffractogram 1) exhibited two small peaks at  $2\theta = 20.15^\circ$  and  $23.41^\circ$ , assigned to the crystal lattice planes 200 and 002/202 of the  $\alpha$ -crystalline form of PA6 (JCPDS: 022-0700). Two intense peaks were observed at  $2\theta = 43.10^\circ$  and  $53.10^\circ$ , corresponding to the 111 and 200 crystal lattice planes of metallic copper, respectively. These results are consistent with JCPDS: 003-1018.



**Figure 16.** XRD diffractogram of samples: (1) PA/Cu; (2) PA/Cu/Bi-S. The peaks are labelled as follows:  $\Delta$ —PA6 (JCPDS: 022-0700);  $\blacktriangledown$ —Cu (JCPDS: 003-1018).

Despite the colour changing from copper-coloured to black after thin films of  $\text{Bi}_2\text{S}_3$  were deposited, the XRD patterns of the PA/Cu/Bi-S composite (Figure 16, diffractogram 2) did not detect any peaks assigned to the  $\text{Bi}_2\text{S}_3$  phase, except for those assigned to PA6 of the untreated PA/Cu sample. The Cu peaks had disappeared. The absence of peaks is probably due to the formation of an amorphous phase or very small crystallites. The small size of these crystallites reduces the scattering power of the incident X-ray beam, resulting in the disappearance of peaks in the diffraction pattern.

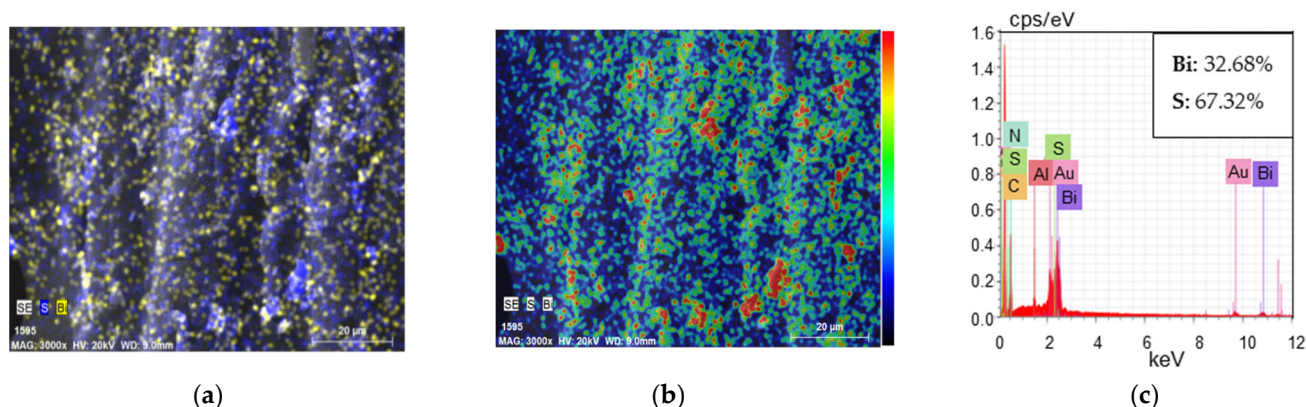
Figure 17 shows SEM images of the deposited  $\text{Bi}_2\text{S}_3$  thin film onto PA/Cu.  $\text{Bi}_2\text{S}_3$  coated the surface of PA/Cu individual strands. After further magnification, it is visible that the thin film is not evenly deposited, with some deficit areas. Structures formed vary in size (250–900 nm) and shape, including a layer of fine nanostars and individual larger nanoflakes.



**Figure 17.** SEM images of PA/Cu/Bi-S composite: (a) 300 $\times$  magnified; (b) 40,000 $\times$  magnified.



Spatial and concentration distributions of bismuth and sulphur on PA/Cu are shown in Figure 18. Spatial distribution (Figure 18a) shows an evenly spread-out sulphur layer that covers the surface with sparse spots of bismuth, some of them forming larger structures. This is supported by concentration distribution (Figure 18b), as there are spots of higher concentration, surrounded by dark blue areas.

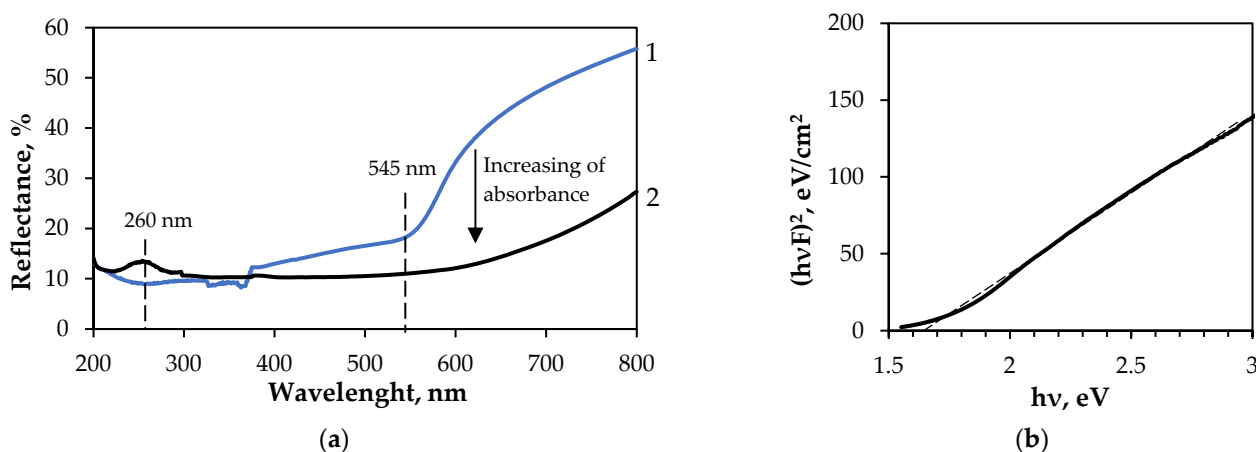


**Figure 18.** EDX elemental maps of Bi (yellow) and sulphur (blue) ( $10,000\times$  magnified) of PA/Cu/Bi-S surface: (a) spatial distribution of elements; (b) elemental concentration distribution; (c) representative EDX spectra. The normalised atomic percentages of Bi and S in the films are shown in the corresponding inset.

As can be seen from the representative EDX spectra (shown as an inset in Figure 18c), the normalised atomic percentages of bismuth and sulphur are 32.68% and 67.32%, respectively. These values are very close to those obtained for the C/PES/S/Bi-S samples and tend to approach stoichiometry.

The reflectance spectrum of nylon fabric can vary depending on factors such as the type of nylon, its surface treatment and whether it is coated or dyed. Nylon generally has high reflectivity in the near-infrared (NIR) range, with untreated nylon reflecting up to 90% of NIR radiation. However, due to its chemical structure, which includes amide groups (N-H) and carbonyl groups (C=O), PA6 fabric can absorb UV radiation through electronic transitions. Absorption in the 270–300 nm region is common for molecules containing a C=O group, corresponding to an  $n\rightarrow\pi^*$  transition. Nylon typically absorbs UV radiation, particularly in the 290–315 nm range [64]. In the NIR region, the diffuse reflectance of copper thin films tends to increase with wavelengths above 600 nm. Thicker films generally exhibit higher reflectance [65]. The presence of copper additives in the PA/Cu textile sample indicates a change in its optical properties of neat PA6. Consequently, the sample exhibits an absorption maximum at 260 nm, with a reflectance of 9% (see Figure 19a, spectrum 1). Reflectance then increases stepwise from 260 nm to 550 nm, reaching 18%. Further reflectance shows an even stronger increase, reaching 55% at 800 nm. This is lower than that of woven fabrics, where the yarns are often interwoven. As the studied PA/Cu textile is a knitted fabric, the pores between the yarns are generally larger, which suggests lower reflectance. After the deposition of a thin film of bismuth sulphide, the deposited materials covered the individual yarns and reduced the pores. Consequently, the reflectance in the region from 200 nm to 550 nm was approximately 10%, except for a slight increase to 13% at 260 nm (Figure 19a, spectrum 2). In the spectral region beyond 550 nm, reflection slowly increases, reaching 27% at 800 nm. The  $E_g$  value for the PA/Cu/Bi-S composite is 1.68 eV, as shown in Figure 19b. This was determined by plotting the linear fit and the photon energy axis.

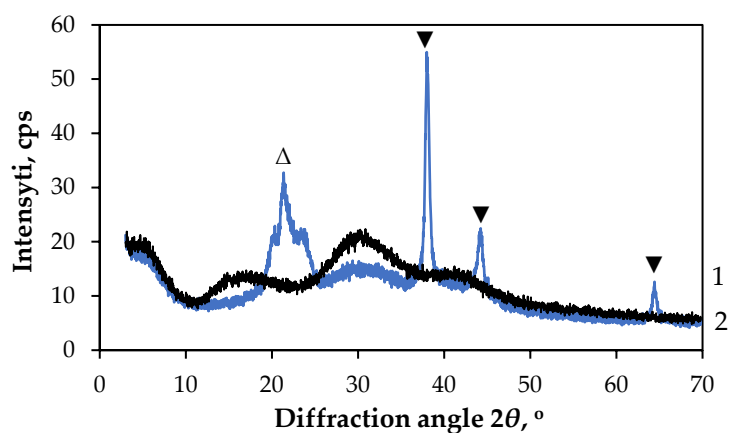




**Figure 19.** (a) Optical reflectance spectra as a function of the wavelength in the range of 200–800 nm for samples: (1) PA/Cu; (2) PA/Cu/Bi-S. (b)  $E_g$  determination for PA/Cu/Bi-S by Kubelka–Munk method.

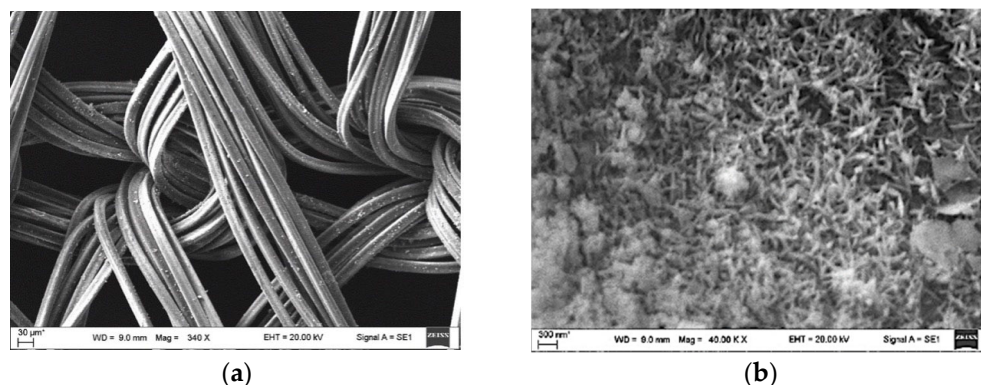
### 3.2.5. Characterisation of PA/Ag/Bi-S Samples

The PA/Ag textile was produced by coating the surface of the PA6 fibre fabric with silver nanoparticles. The diffraction patterns of the PA/Ag samples (Figure 20, diffractogram 1) exhibited one peak at  $2\theta = 21.38^\circ$ . Specifically, in JCPDS 12-923, this peak is attributed to the (001) crystal lattice plane of the  $\gamma$ -phase of PA6. Three additional peaks of different intensity were also registered at  $2\theta = 37.98^\circ$ ,  $44.18^\circ$ , and  $64.37^\circ$ , which correspond to the 111, 200, and 220 face-centred cubic silver crystal lattice planes (JCPDS: 04-0783), respectively.



**Figure 20.** XRD diffractogram of samples: (1) PA/Ag; (2) PA/Ag/Bi-S. The peaks are labelled as follows:  $\Delta$ —PA6 (JCPDS: 12-923);  $\blacktriangledown$ —Ag (JCPDS: 04-0783).

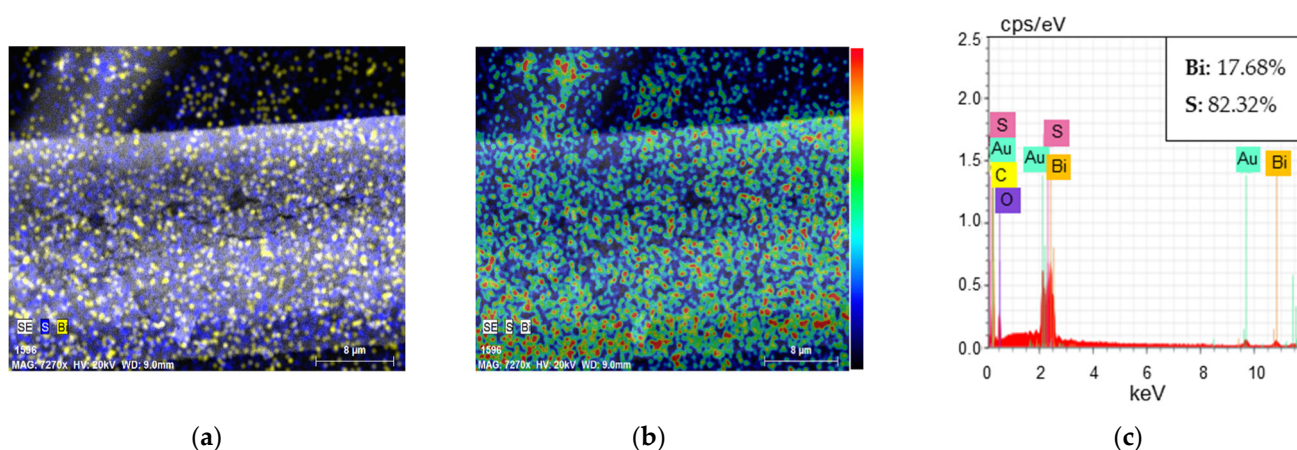
The XRD patterns of the PA/Ag/Bi-S composite (Figure 20, diffractogram 2) show that all the initial peaks registered for the PA/Ag samples disappeared. Three broad peaks, with maxima at approximately  $2\theta = 15.6^\circ$ ,  $30.9^\circ$  and  $41.2^\circ$ , were registered on the diffractogram. As can be seen in Figure 21a, the PA/Ag textile consists of yarns. It is elastic and has small holes called eyelets. It can therefore be assumed that, during the formation of bismuth sulphide, the precursor solutions penetrated the knitted fabric and the precipitated materials coated the yarns. The presence of these broad peaks indicates an absence of a defined crystal structure, with only short-range order present.



**Figure 21.** SEM images of PA/Ag/Bi-S composite: (a) 300x magnified; (b) 40,000× magnified.

Figure 21 shows SEM images of a deposited  $\text{Bi}_2\text{S}_3$  thin film on a PA/Ag textile. The film coated the individual yarns of fabric evenly, with no visible imperfections (Figure 21a). Figure 21b shows an evenly deposited layer consisting of differently shaped structures, including fine nanostars and larger nanoflakes (150–600 nm). Cracks or pores are not visible.

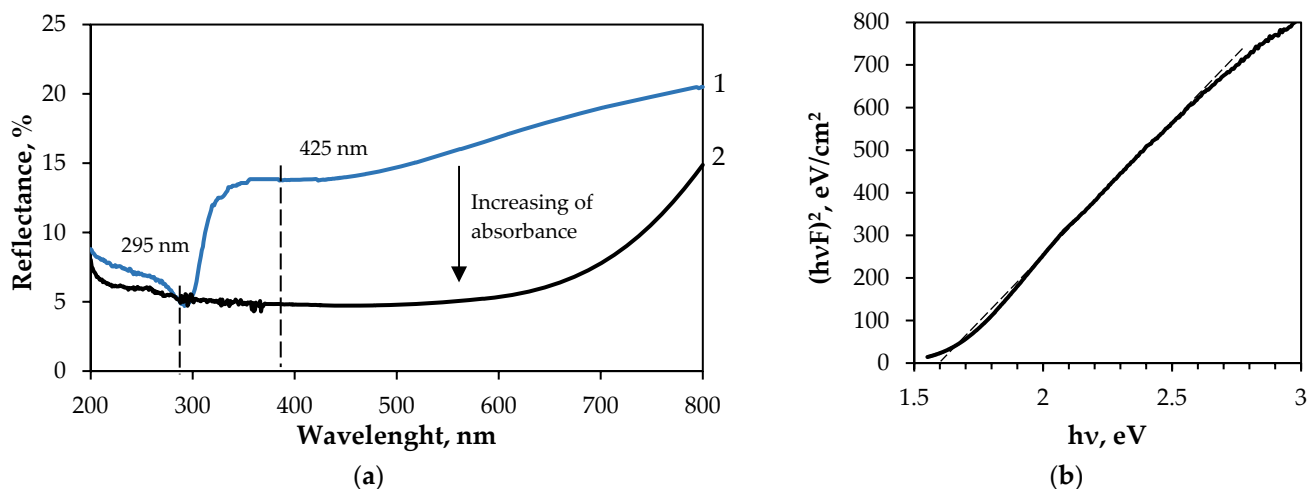
Spatial and concentration distributions of bismuth and sulphur, on PA/Ag, obtained by EDX, are shown in Figure 22. Spatial distribution (Figure 22a) provides the information that sulphur is more evenly distributed and that bismuth forms either smaller or larger clusters that result in nanostructures of differing size and shape. The results are supported in Figure 22b, as there are areas indicating a surplus of elements. Representative EDX spectra (see inset in Figure 22c) show the normalised atomic percentages of bismuth and sulphur to be 17.68% and 82.32%, respectively. These differ from the results obtained for composites C/PES/S/Bi-S and PA/Cu/Bi-S, and demonstrate that the obtained films are rich in sulphur.



**Figure 22.** EDX elemental maps of Bi (yellow) and sulphur (blue) (10,000× magnified) of PA/Ag/Bi-S surface: (a) spatial distribution of elements; (b) elemental concentration distribution; (c) representative EDX spectra. The normalised atomic percentages of Bi and S in the films are shown in the corresponding inset.

Figure 23 shows the UV–Vis DR spectra of the PA/Ag textile samples, as well as the PA/Ag/Bi-S composite. As mentioned above, nylon PA6 fabric has characteristic absorption peaks in the UV region, typically in the 290–315 nm range. Therefore, the absorption peak at 295 nm we attribute to the PA6. The metallic grey colour of the sample, resembling silver, suggests a change in its optical properties. Depending on their size, shape and distribution in nanostructures, monodisperse silver nanoparticles have two absorption bands: a broad peak in the range of 420–430 nm and a shoulder at 580–590 nm [66]. Therefore, a

broad absorption peak, with a maximum at 425 nm, can be attributed to a small quantity of silver nanoparticles.



**Figure 23.** (a) Optical reflectance spectra as a function of the wavelength in the range of 200–800 nm for samples: (1) PA/Ag; (2) PA/Ag/Bi-S. (b)  $E_g$  determination for PA/Ag/Bi-S by Kubelka–Munk method.

As shown in Figure 23, spectrum 2, absorption of the samples increased after deposition of the  $\text{Bi}_2\text{S}_3$  thin films, reaching approximately 95% in the 200–600 nm region. There was also an absorption decrease in the visible and near-infrared regions. At 800 nm, the absorption level was 85%. We determined the  $E_g$  value for the PA/Ag/Bi-S composite to be 1.6 eV by intersecting the linear fit with the photon energy axis (see Figure 23b).

#### 4. Conclusions

The main objective of this study was to synthesise  $\text{Bi}_2\text{S}_3$  semiconductor thin films on various flexible textiles simultaneously using the SILAR method. In the absence of a complexing agent,  $\text{Na}_2\text{S}_2\text{O}_3$  was used as the sulphur precursor. The influence of textile composition on the phase composition, surface morphology and optical properties of the deposited films was investigated. A comparison of the results obtained in the present study is shown in Table 3.

**Table 3.** Comparison of structural, morphological and optical results of obtained composites.

Composite	Bi/S Ratios <sup>1</sup>	Crystallinity	$E_g$ , eV
GF/PTFE/Bi-S	0.038	Polycrystalline orthorhombic $\text{Bi}_2\text{S}_3$	1.8
PET/PVC/Bi-S	0.044	Polycrystalline orthorhombic $\text{Bi}_2\text{S}_3$ , monoclinic sulphur $\text{S}_8$	1.68
C/PES/S/Bi-S	0.512	Orthorhombic $\text{Bi}_2\text{S}_3$	1.58
PA/Cu/Bi-S	0.485	Amorphous phase or very small crystallites of $\text{Bi}_2\text{S}_3$	1.68
PA/Ag/Bi-S	0.215	Absence of a defined crystal structure, with only short-range order present	1.6

<sup>1</sup> The stoichiometric ratio of Bi/S is 0.67.

As can be seen, the substrate strongly influenced the crystal structure of the film, the Bi/S ratio, and the optical energy gap. The interaction between the film and the substrate also plays a role. For example, increasing the average grain size of a GF/PTFE surface after etching reduced the available surface area for deposition, thereby altering the surface's reactivity for thin film deposition by creating fewer nucleation sites. This

trapped reactants and hindered coverage. Consequently, the layer of  $\text{Bi}_2\text{S}_3$  was very thin. The excess of sulphur in some films can be interpreted in terms of the surface properties of the textile being studied, such as its density and porosity, as well as the properties of thiosulfate ions. The diffusion properties of  $\text{S}_2\text{O}_3^{2-}$  ions in aqueous solutions indicate a characteristic translational diffusion length of approximately 2 nm over a given time period [67]. While the porosity of these surfaces was small, the radius of  $\text{S}_2\text{O}_3^{2-}$  ions with a tetragonal structure was high, and the surfaces of these textile samples were supersaturated with  $\text{S}_2\text{O}_3^{2-}$  ions. Thiosulfate ions in acidic  $\text{Bi}(\text{NO}_3)_3$  solution, due to hydrolysis, give various sulphur rings [68]. Consequently, a high concentration of sulphur was found on the surfaces of the GF/PTFE/Bi-S and PET/PVC/Bi-S composite materials. The Bi/S ratios were found to be 0.038 and 0.044, respectively. In other textile materials (C/PES/S, PA/Ag and PA/Cu) that are more porous,  $\text{S}_2\text{O}_3^{2-}$  ions can penetrate deeper into the textile matrix and react with  $\text{Bi}^{3+}$  ions to form  $\text{Bi}_2\text{S}_3$ . Therefore, the composites obtained consist of an amorphous phase or very small crystallites of orthorhombic  $\text{Bi}_2\text{S}_3$ . A very significant increase was seen in the Bi/S ratios. SEM analysis revealed that  $\text{Bi}_2\text{S}_3$  films did not grow uniformly; rather, they formed individual agglomerates of nanoparticles at specific locations, gradually covering the entire textile surface with each subsequent deposition cycle. The resulting bismuth sulphide nanostructures depend on the textile used and can take the form of stars, spheres, snowflakes or flowers. EDX spectroscopy was used to confirm the distribution of bismuth (Bi) and sulphur (S) within the nanoparticles and agglomerates. These elements were found to be concentrated in the top layers of the films. They may have been present at different concentrations in the textile matrix. Secondary electrons (SEs), on the other hand, typically originate from within a few nanometres of the sample surface [69]. Additionally, EDX analysis revealed elevated levels of sulphur in the  $\text{Bi}_2\text{S}_3$  films on individual textile samples. In its monoclinic form, sulphur is not a constituent of standard PV cells. However, it can be used in combination with other materials to produce components for energy storage, which could potentially impact PV technology indirectly [70,71]. The presence of sulphur impurities in  $\text{Bi}_2\text{S}_3$  thin films did not significantly affect the optical energy gap values. Optical characterisation revealed that the deposited films are optical energy gap semiconductors with an  $E_g$  ranging from 1.58 to 1.8 eV. Future research should focus on selecting suitable textiles to produce semiconductor films with an appropriate optical energy gap that do not require annealing for use in manufacturing flexible photovoltaic materials. Thus, the formation of thin bismuth(III) sulphide films simultaneously on various textile substrates with a low optical energy gap value should be of interest for many applications due to the simplicity and low cost of the process.

**Author Contributions:** Conceptualisation, V.K.; methodology, V.K. and V.S.; software, V.S.; formal analysis, V.S.; investigation, V.K.; data curation, V.K.; writing—original draft preparation, V.K.; supervision, V.K.; funding acquisition, V.K. All authors have read and agreed to the published version of the manuscript.

**Funding:** This research was funded by the Lithuanian Research Council through its funding of student research and internships, Grant No. S-ST-23-64.

**Data Availability Statement:** The original contributions presented in this study are included in the article. Further inquiries can be directed to the corresponding author(s).

**Acknowledgments:** The authors would like to thank student E. Skuodaite from the Kaunas University of Technology for her help with the experiments.

**Conflicts of Interest:** The authors declare no conflicts of interest.



## References

- Ojstršek, A.; Plohl, O.; Gorgieva, S.; Kurečič, M.; Jančič, U.; Hribernik, S.; Fakin, D. Metallisation of textiles and protection of conductive layers: An overview of application techniques. *Sensors* **2021**, *21*, 3508. [\[CrossRef\]](#)
- Zhong, H.; Bai, Z.; Zou, B. Tuning the luminescence properties of colloidal I-III-VI semiconductor nanocrystals for optoelectronics and biotechnology applications. *J. Phys. Chem. Lett.* **2012**, *3*, 3167–3175. [\[CrossRef\]](#)
- Talapin, D.V.; Lee, J.S.; Kovalenko, M.V.; Shevchenko, E.V. Prospects of colloidal nanocrystals for electronic and optoelectronic applications. *Chem. Rev.* **2010**, *110*, 389–458. [\[CrossRef\]](#)
- Manimegalai, D.K.; Manikandan, A.; Moortheswaran, S.; Antony, S.A. One-pot microwave irradiation synthesis and characterization studies of nanocrystalline CdS photocatalysts. *Adv. Sci. Eng. Med.* **2015**, *7*, 722–727. [\[CrossRef\]](#)
- Manikandan, A.; Antony, S.A. A novel approach for the synthesis and characterization studies of Mn<sup>2+</sup>-Doped CdS nano-crystals by a facile microwave-assisted combustion method. *J. Supercond. Nov. Magn.* **2014**, *27*, 2725–2733. [\[CrossRef\]](#)
- Reneka Deves, D.; Sivanesan, T.; Muthukrishnan, R.M.; Pourkodee, D.; Mohammed Yusuf Ansari, P.; Abdul Kader, S.M.; Raniyani, R.A. A novel photocatalytic activity of Bi<sub>2</sub>S<sub>3</sub> nanoparticles for pharmaceutical and organic pollution removal in water remediation. *Chem. Phys. Impact* **2024**, *8*, 100605. [\[CrossRef\]](#)
- Onwudiwe, D.C.; Nkwe, V.M. Morphological variations in Bi<sub>2</sub>S<sub>3</sub> nanoparticles synthesized by using single source precursor. *Heliyon* **2020**, *6*, e04505. [\[CrossRef\]](#)
- Razavi, F.S.; Mahdi, M.A.; Ghanbari, D.; Dawi, E.A.; Abed, M.J.; Ganduh, S.H.; Jasmin, L.S.; Salavati-Niasari, M. Fabrication and design of four-component Bi<sub>2</sub>S<sub>3</sub>/CuFe<sub>2</sub>O<sub>4</sub>/Cu<sub>2</sub>O nanocomposite as new active materials for high performance electrochemical hydrogen storage application. *J. Energy Storage* **2024**, *94*, 113493. [\[CrossRef\]](#)
- Yu, Y.; Hu, Z.; Lien, S.Y.; Yu, Y.; Gao, P. Self-powered thermoelectric hydrogen sensors based on low-cost bismuth sulphide thin films: Quick response at room temperature. *ACS Appl. Mater. Interfaces* **2022**, *14*, 47696–47705. [\[CrossRef\]](#)
- Kan, H.; Yang, W.; Guo, Z.; Li, M. Highly sensitive room-temperature NO<sub>2</sub> gas sensor based on Bi<sub>2</sub>S<sub>3</sub> nanorods. *J. Mater. Sci. Mater. Electron.* **2024**, *35*, 331. [\[CrossRef\]](#)
- Rong, P.; Gao, S.; Ren, S.; Lu, H.; Yan, J.; Li, L.; Zhang, M.; Han, Y.; Jiao, S.; Wang, J. Large-area freestanding Bi<sub>2</sub>S<sub>3</sub> nanofibrous membranes for fast photoresponse flexible IR imaging photodetector. *Adv. Funct. Mater.* **2023**, *33*, 2300159. [\[CrossRef\]](#)
- Singh, A.; Chauhan, P.; Verma, A.; Yadav, B.C. Interfacial engineering enables polyaniline-decorated bismuth sulphide nanorods towards ultrafast metal-semiconductor-metal UV-Vis broad spectra photodetector. *Adv. Compos. Hybrid Mater.* **2024**, *7*, 88. [\[CrossRef\]](#)
- Zhang, X.; Xie, J.; Tang, Y.; Lu, Z.; Hu, J.; Wang, Y.; Cao, Y. Oxygen self-doping Bi<sub>2</sub>S<sub>3</sub>@C spheric successfully enhanced long-term performance in lithium-ion batteries. *ACS Appl. Mater. Interfaces* **2024**, *16*, 52423–52431. [\[CrossRef\]](#) [\[PubMed\]](#)
- Terdalkar, P.; Kumbhar, D.D.; Pawar, S.D.; Nirmal, K.A.; Kim, T.G.; Mukherjee, S.; Khot, K.V.; Dongale, T.D. Revealing switching statistics and artificial synaptic properties of Bi<sub>2</sub>S<sub>3</sub> memristor. *Solid State Electron.* **2025**, *225*, 109076. [\[CrossRef\]](#)
- Zhao, Y.; Tao, Y.; Huang, Q.; Huang, J.; Kuang, J.; Gu, R.; Zeng, P.; Li, H.-Y.; Liang, H.; Liu, H. Electrochemical Biosensor Employing Bi<sub>2</sub>S<sub>3</sub> Nanocrystals-Modified Electrode for Bladder Cancer Biomarker Detection. *Chemosensors* **2022**, *10*, 48. [\[CrossRef\]](#)
- Yang, Z.; Wang, L.; Zhang, J.; Liu, J.; Yu, X. Application of bismuth sulphide based nanomaterials in cancer diagnosis and treatment. *Nano Today* **2023**, *49*, 101799. [\[CrossRef\]](#)
- Liang, K.; Wang, C. Capacitive and photocatalytic performance of Bi<sub>2</sub>S<sub>3</sub> nanostructures synthesized by solvothermal method. *Phys. Lett. A* **2017**, *38*, 652–657. [\[CrossRef\]](#)
- Supekar, A.T.; Bhujbal, P.K.; Salunke, S.A.; Rathod, S.M.; Patole, S.P.; Pathan, H.M. Bismuth sulphide and antimony sulphide-based solar cells: A review. *ES Energy Environ.* **2023**, *19*, 848. [\[CrossRef\]](#)
- Yu, X.L.; Cao, C.B. Photoresponse and field-emission properties of bismuth sulphide nanoflowers. *Cryst. Growth Des.* **2008**, *8*, 3951–3955. [\[CrossRef\]](#)
- Yu, Y.; Jin, C.H.; Wang, R.H.; Chen, Q.; Peng, L.M. High-quality ultralong Bi<sub>2</sub>S<sub>3</sub> nanowires: Structure, growth, and properties. *J. Phys. Chem.* **2005**, *109*, 18772–18776. [\[CrossRef\]](#)
- Ajiboye, T.O.; Onwudiwe, D.C. Bismuth sulphide based compounds: Properties, synthesis and applications. *Results Chem.* **2021**, *3*, 100151. [\[CrossRef\]](#)
- Onwudiwe, D.C.; Oyewo, O.A.; Atamtürk, U.; Ojelere, O.; Mathur, S. Photocatalytic reduction of Cr(VI) using star-shaped Bi<sub>2</sub>S<sub>3</sub> obtained from microwave irradiation of bismuth complex. *J. Environ. Chem. Eng.* **2020**, *8*, 103816. [\[CrossRef\]](#)
- Zhang, M.; Chen, D.J.; Wang, R.Z.; Feng, J.J.; Bai, Z.; Wang, A.J. D-penicillanime assisted hydrothermal synthesis of Bi<sub>2</sub>S<sub>3</sub> nanoflowers and their electrochemical application. *Mater. Sci. Eng.* **2013**, *33*, 3980–3985. [\[CrossRef\]](#)
- Linhart, W.M.; Zelewski, S.J.; Scharoch, P.; Dybała, F.; Kudrawiec, R. Nesting-like band gap in bismuth sulphide Bi<sub>2</sub>S<sub>3</sub>. *J. Mater. Chem. C* **2021**, *9*, 13733–13738. [\[CrossRef\]](#)
- Ran, Y.; Song, Y.; Jia, X.; Gu, P.; Cheng, Z.; Zhu, Y.; Wang, Q.; Pan, Y.; Li, Y.; Gao, Y.; et al. Large-Scale Vertically Interconnected Complementary Field-Effect Transistors Based on Thermal Evaporation. *Small* **2024**, *20*, 2309953. [\[CrossRef\]](#) [\[PubMed\]](#)



26. Atamturk, U.; Jung, E.; Fischer, T.; Mathur, S. Tale of Two Bismuth Alkylthiolate Precursors' Bifurcating Paths in Chemical Vapor Deposition. *Chem. Mater.* **2022**, *34*, 7344–7356. [\[CrossRef\]](#)
27. Tezcan, F. A new synthesis route of Bi<sub>2</sub>S<sub>3</sub> with solvothermal deposition in photoelectrochemical hydrogen production. *J. Mol. Struct.* **2024**, *1301*, 137418. [\[CrossRef\]](#)
28. Parra-Arciniega, S.M.; Garcia-Gomez, N.A.; Garza-Toyar, L.L.; García-Gutiérrez, D.I.; Sánchez, E.M. Ultrasonic irradiation-assisted synthesis of Bi<sub>2</sub>S<sub>3</sub> nanoparticles in aqueous ionic liquid at ambient condition. *Ultrason. Sonochemistry* **2017**, *36*, 95–100. [\[CrossRef\]](#) [\[PubMed\]](#)
29. Rodriguez-Rosales, K.; Cruz-Gomez, J.; Cruz, J.S.; Guillen-Cervantes, A.; de Moure-Flores, F.; Villagran-Muniz, M. Plasma emission spectroscopy for studying Bi<sub>2</sub>S<sub>3</sub> produced by pulsed laser deposition and effects of substrate temperature on structural, morphological, and optical properties of thin films. *Mater. Sci. Eng. B* **2025**, *312*, 117867. [\[CrossRef\]](#)
30. Bouachri, M.; Oubakalla, M.; El Farri, H.; Diaz-Guerra, C.; Mhalla, J.; Zimou, J.; El-Habib, A.; Beraich, M.; Nouneh, K.; Fahoume, M.; et al. Substrate temperature effects on the structural, morphological and optical properties of Bi<sub>2</sub>S<sub>3</sub> thin films deposited by spray pyrolysis: An experimental and first-principles study. *Opt. Mater.* **2023**, *135*, 113215. [\[CrossRef\]](#)
31. Grubač, Z.; Metikoš-Huković, M. Electrodeposition of thin sulphide films: Nucleation and growth observed for Bi<sub>2</sub>S<sub>3</sub>. *Thin Solid Films* **2002**, *412*, 248–256. [\[CrossRef\]](#)
32. Castillo-Carillo, A.; Rivas-Valles, B.G.; Castillo, S.J.; Ramirez, M.M.; Luque-Morales, P.A. New formulation to synthesize semiconductor Bi<sub>2</sub>S<sub>3</sub> thin films using chemical bath deposition for optoelectronic applications. *Chem. Sym.* **2022**, *14*, 2487. [\[CrossRef\]](#)
33. Raut, S.S.; Dhobale, J.A.; Sankapal, B.R. SILAR deposited Bi<sub>2</sub>S<sub>3</sub> thin film toward electrochemical supercapacitor. *Phys. E* **2017**, *87*, 209–212. [\[CrossRef\]](#)
34. Selmane, N.; Eddine, H. Effect of complexing agent on the structural properties of bismuth sulphide Bi<sub>2</sub>S<sub>3</sub> thin films prepared by chemical bath deposition technique. *Rev. Sci. Sci. L'ingénieur* **2010**, *1*, 22–26.
35. Fazal, T.; Iqbal, S.; Shah, M.; Ismail, B.; Shaheen, N.; Alharthi, A.I.; Awwad, N.S.; Ibrahim, H.A. Correlation between structural, morphological and optical properties of Bi<sub>2</sub>S<sub>3</sub> thin films deposited by various aqueous and non-aqueous chemical bath deposition methods. *Results Phys.* **2022**, *40*, 105817. [\[CrossRef\]](#)
36. Alaburdaitė, R.; Krylova, V. Polypropylene film surface modification for improving its hydrophilicity for innovative applications. *Polym. Degrad. Stab.* **2023**, *211*, 110334. [\[CrossRef\]](#)
37. Nasr, M.; Viter, R.; Eid, C.; Warmont, F.; Habchi, R.; Miele, P.; Bechelany, M. Synthesis of novel ZnO/ZnAl<sub>2</sub>O<sub>4</sub> multi co-centric nanotubes and their long-term stability in photocatalytic application. *RSC Adv.* **2016**, *6*, 103692–103699. [\[CrossRef\]](#)
38. López, R.; Gómez, R. Band-gap energy estimation from diffuse reflectance measurements on sol-gel and commercial TiO<sub>2</sub>: A comparative study. *J. Sol-Gel Sci. Technol.* **2012**, *61*, 1–7. [\[CrossRef\]](#)
39. Asrafali, S.P.; Periyasamy, T.; Kim, S.C. Hydrophilic Nature of Polytetrafluoroethylene through Modification with Perfluorosulfonic Acid-Based Polymers. *Sustainability* **2023**, *15*, 16479. [\[CrossRef\]](#)
40. Pugmire, D.L.; Wetteland, C.J.; Duncan, W.S.; Lakis, R.E.; Schwartz, D.S. Cross-linking of polytetrafluoroethylene during room-temperature irradiation. *Polym. Degrad. Stab.* **2009**, *94*, 1533–1541. [\[CrossRef\]](#)
41. Liu, Q.; Shi, J.; Sun, J.; Wang, T.; Zeng, L.; Jiang, G. Graphene and graphene oxide sheets supported on silica as versatile and high-performance adsorbents for solid-phase extraction. *Angew. Chem. Int. Ed.* **2011**, *50*, 5913–5917. [\[CrossRef\]](#)
42. Krylova, V.; Dukštienė, N.; Lelis, M.; Tučkutė, S. PES/PVC textile surface modification by thermo-chemical treatment for improving its hydrophilicity. *Surf. Interfaces* **2021**, *25*, 101184. [\[CrossRef\]](#)
43. Xia, L.; Zhang, Q.; Zhuang, X.; Zhang, S.; Duan, C.; Wang, X.; Cheng, B. Hot-pressed wet-laid polyethylene terephthalate nonwovens as support for separation membranes. *Polymers* **2019**, *11*, 1547. [\[CrossRef\]](#)
44. Kormunda, M.; Pavlik, J. Characterization of oxygen and argon ion flux interaction with PET surfaces by in-situ XPS and ex-situ FTIR. *Polym. Degrad. Stab.* **2010**, *95*, 1783–1788. [\[CrossRef\]](#)
45. Zhang, H.; Li, X.; Mao, N.; Sun, R.; Xu, J. Fabrication of magnetized polyester fabric grafted with β-cyclodextrin for controlled release of menthol. *J. Ind. Text.* **2016**, *47*, 1060–1082. [\[CrossRef\]](#)
46. Moros, J.; Cassella, R.J.; Barciela-Alonso, M.C.; Moreda-Pineiro, A.; Herbello-Hermelo, P.; Bermejo-Barrera, P. Estuarine sediment quality assesment by Fourier-transform infrared spectroscopy. *Vib. Spectrosc.* **2010**, *53*, 204–213. [\[CrossRef\]](#)
47. Mina, M.S.; Kabir, H.; Rahman, M.M.; Kabir, M.A.; Rahaman, M.; Bashir, M.S.; Islam, M.S.; Sharmin, A.; Ahmed, F. Optical and Morphological Characterization of BaSe Thin Films Synthesized via Chemical Bath Deposition. *IOSR J. Appl. Phys.* **2013**, *4*, 30–35. [\[CrossRef\]](#)
48. Si, J.; Ma, R.; Wu, Y.; Dong, Y. Microstructure and magnetic properties of novel powder cores composed of iron-based amorphous alloy and PTFE. *J. Mater. Sci.* **2022**, *57*, 8154–8166. [\[CrossRef\]](#)
49. Hu, X.; Zhang, Q.; Yu, H.; Zhao, D.; Dong, S.; Zhou, Q. Quantitative analysis of naturally colored cotton and white cotton blends by UVvis diffuse reflectance spectroscopy. *J. Appl. Spect.* **2015**, *81*, 949–955. [\[CrossRef\]](#)

50. Essaidia, H.; Gantassi, A.; Touihria, S.; Ouerfelli, J. Tuning the structural, optical and electrical properties of AgInSe<sub>2</sub> thin films prepared by sequentially deposited silver and indium nano-films under vacuum. *Optik* **2019**, *182*, 866–875. [\[CrossRef\]](#)
51. Rincón, M.E.; Campos, J.; Suárez, R. A comparison of the various thermal treatments of chemically deposited bismuth sulfide thin films and the effect on the structural and electrical properties. *J. Phys. Chem. Solids* **1999**, *60*, 385–392. [\[CrossRef\]](#)
52. Gao, C.; Shen, H.; Sun, L.; Shen, Z. Chemical bath deposition of Bi<sub>2</sub>S<sub>3</sub> films by a novel deposition system. *Appl. Surf. Sci.* **2011**, *257*, 7529–7533. [\[CrossRef\]](#)
53. Li, Z.; Si, G.; Ning, Z.; Liu, J.; Fang, Y.; Si, B.; Cheng, Z.; Yang, C. Highly Sensitive Sphere-Tube Coupled Photoacoustic Cell Suitable for Detection of a Variety of Trace Gases: NO<sub>2</sub> as an Example. *Sensors* **2022**, *22*, 281. [\[CrossRef\]](#) [\[PubMed\]](#)
54. Dutta, A.K.; Maji, S.K.; Mitra, K.; Sarkar, A.; Saha, N.; Ghosh, A.B.; Adhikary, B. Single source precursor approach to the synthesis of Bi<sub>2</sub>S<sub>3</sub> nanoparticles: A new amperometric hydrogen peroxide biosensor. *Sens. Actuators B Chem.* **2024**, *192*, 578–585. [\[CrossRef\]](#)
55. Achwal, W.B. Sun protection properties of textile substrates. *Colorage* **1997**, *44*, 31–32.
56. Abdel-Fattah, E.; Alharthi, A.I.; Fahmy, T. Spectroscopic, optical and thermal characterization of polyvinyl chloride-based plasma-functionalized MWCNTs composite thin films. *Appl. Phys. A* **2019**, *125*, 475. [\[CrossRef\]](#)
57. Sun, S.; Ding, H.; Hou, X. Preparation of CaCO<sub>3</sub>-TiO<sub>2</sub> composite particles and their pigment properties. *Materials* **2018**, *11*, 1131. [\[CrossRef\]](#)
58. da Silva, D.J.; Escote, M.T.; Cruz, S.A.; Simião, D.F.; Zenatti, A.; Curvello, M.S. Polycarbonate/TiO<sub>2</sub> nanofibers nanocomposite: Preparation and properties. *Polym. Compos.* **2018**, *39*, 780–790. [\[CrossRef\]](#)
59. Acharya, S.; Hu, Y.; Abidi, N. Cellulose Dissolution in Ionic Liquid under Mild Conditions: Effect of Hydrolysis and Temperature. *Fibers* **2021**, *9*, 5. [\[CrossRef\]](#)
60. Riahi, M.; Martinez-Tomas, C.; Agouram, S.; Boukhachem, A.; Maghraoui-Meherzi, H. The effects of thermal treatment on structural morphological and optical properties of electrochemically deposited Bi<sub>2</sub>S<sub>3</sub> thin films. *Thin Solid Films* **2017**, *626*, 9–16. [\[CrossRef\]](#)
61. Sonawane, P.S.; Patil, L.A. Effect of nonstoichiometry on structural and optical properties of nanostructured Bi<sub>2</sub>S<sub>3</sub> thin films prepared chemically at room temperature. *Mater. Chem. Phys.* **2007**, *105*, 157–161. [\[CrossRef\]](#)
62. Goncalves, G.; Marques, P.A.; Pinto, R.J.; Trindade, T.; Neto, C.P. Surface modification of cellulosic fibres for multipurpose TiO<sub>2</sub> based nanocomposites. *Compos. Sci. Technol.* **2009**, *69*, 7–8. [\[CrossRef\]](#)
63. Bai, C.; Yuan, X.; Cao, Y.; Hao, Z.; Pan, L.; Peng, J.; Liu, N.; Chen, S. Perdurable antimicrobial and ultraviolet-blocking cotton fabric by one-step eco-friendly strategy. *Ind. Crop. Prod.* **2025**, *223*, 120038. [\[CrossRef\]](#)
64. Das, B.R. UV Radiation Protective Clothing. *The Op. Text. J.* **2010**, *3*, 14–21.
65. Foadi, F.; Etminan, M.; Aghamir, F.M.; Mohammadizadeh, M.R. Role of surface morphological parameters on wettability of obliquely deposited Cu thin films in a plasma focus device. *J. Mater. Res.* **2023**, *38*, 3666–3676. [\[CrossRef\]](#)
66. Singh, S.; Bharti, A.; Meena, V.K. Green synthesis of multi-shaped silver nanoparticles: Optical, morphological and antibacterial properties. *J. Mater. Sci. Mater. Electron.* **2015**, *26*, 3638–3648. [\[CrossRef\]](#)
67. Reichenbach, J.; Klaas, W. Frustration vs Prenucleation: Understanding the Suprising Stability of Supersaturated Sodium Thiosulfate Solutions. *J. Phys. Chem. B* **2018**, *122*, 7590–7596. [\[CrossRef\]](#)
68. Steudel, R. Homocyclic Sulfur Molecules. *Top. Curr. Chem.* **1982**, *102*, 149–176. [\[CrossRef\]](#)
69. Fleck, N.; Amlı, H.; Dhanak, V.; Ahmed, W. Characterization Techniques in Energy Generation and Storage, Emerging Nanotechnologies for Renewable Energy. In *Micro and Nano Technologies*; Ahmed, W., Booth, M., Nourafkan, E., Eds.; Elsevier: Amsterdam, The Netherlands, 2021; Chapter 11; pp. 259–285, ISBN 9780128213469. [\[CrossRef\]](#)
70. Jung, S.C.; Han, Y.-K. Monoclinic sulfur cathode utilizing carbon for high-performance lithium-sulfur batteries. *J. Power Sources* **2016**, *325*, 495–500. [\[CrossRef\]](#)
71. Moon, S.; Jung, Y.H.; Jung, W.K.; Jung, D.S.; Choi, J.W.; Kim, D.K. Encapsulated Monoclinic Sulfur for Stable Cycling of Li-S Rechargeable Batteries. *Adv. Mater.* **2013**, *25*, 6547–6553. [\[CrossRef\]](#)

**Disclaimer/Publisher’s Note:** The statements, opinions and data contained in all publications are solely those of the individual author(s) and contributor(s) and not of MDPI and/or the editor(s). MDPI and/or the editor(s) disclaim responsibility for any injury to people or property resulting from any ideas, methods, instructions or products referred to in the content.